NASA/TM–2023–104606/Vol. 65

Technical Report Series on Global Modeling and Data Assimilation,
Volume 65

Randal D. Koster, Editor

Validation Assessment for the Soil Moisture Active Passive (SMAP) Level 4 Carbon (L4_C) Data Product Version 7

K. Arthur Endsley, John S. Kimball, Tobias Kundig, Rolf H. Reichle, Joseph V. Ardizzone

June 2023

NASA STI Program ... in Profile

Since its founding, NASA has been dedicated to the advancement of aeronautics and space science. The NASA scientific and technical information (STI) program plays a key part in helping NASA maintain this important role.

The NASA STI program operates under the auspices of the Agency Chief Information Officer. It collects, organizes, provides for archiving, and disseminates NASA's STI. The NASA STI program provides access to the NTRS Registered and its public interface, the NASA Technical Reports Server, thus providing one of the largest collections of aeronautical and space science STI in the world. Results are published in both non-NASA channels and by NASA in the NASA STI Report Series, which includes the following report types:

- TECHNICAL PUBLICATION. Reports of completed research or a major significant phase of research that present the results of NASA Programs and include extensive data or theoretical analysis. Includes compilations of significant scientific and technical data and information deemed to be of continuing reference value. NASA counterpart of peer-reviewed formal professional papers but has less stringent limitations on manuscript length and extent of graphic presentations.

- TECHNICAL MEMORANDUM. Scientific and technical findings that are preliminary or of specialized interest, e.g., quick release reports, working papers, and bibliographies that contain minimal annotation. Does not contain extensive analysis.

- CONTRACTOR REPORT. Scientific and technical findings by NASA-sponsored contractors and grantees.

- CONFERENCE PUBLICATION. Collected papers from scientific and technical conferences, symposia, seminars, or other meetings sponsored or co-sponsored by NASA.

- SPECIAL PUBLICATION. Scientific, technical, or historical information from NASA programs, projects, and missions, often concerned with subjects having substantial public interest.

- TECHNICAL TRANSLATION. English-language translations of foreign scientific and technical material pertinent to NASA's mission.

Specialized services also include organizing and publishing research results, distributing specialized research announcements and feeds, providing information desk and personal search support, and enabling data exchange services.

For more information about the NASA STI program, see the following:

- Access the NASA STI program home page at http://www.sti.nasa.gov

- E-mail your question to help@sti.nasa.gov

- Phone the NASA STI Information Desk at 757-864-9658

- Write to:
  NASA STI Information Desk
  Mail Stop 148
  NASA Langley Research Center
  Hampton, VA 23681-2199

NASA/TM–2023–104606/Vol. 65

Technical Report Series on Global Modeling and Data Assimilation,

Volume 61

Randal D. Koster, Editor

Validation Assessment for the Soil Moisture Active Passive (SMAP) Level 4 Carbon (L4_C) Data Product Version 7

K. Arthur Endsley
University of Montana, Missoula, MT, USA.

John S. Kimball
University of Montana, Missoula, MT, USA.

Tobias Kundig
University of Montana, Missoula, MT, USA.

Rolf H. Reichle
Global Modeling and Assimilation Office, NASA Goddard Space Flight Center, Greenbelt, MD, USA.

Joseph V. Ardizzone
Science Systems and Applications Inc., Lanham, MD, USA.

National Aeronautics and
Space Administration

Goddard Space Flight Center
Greenbelt, Maryland 20771

June 2023

Level of Review: This material has been technically reviewed by technical management.

Available from

NASA STI Program
Mail Stop 148
NASA's Langley Research Center Hampton, VA 23681-2199

National Technical Information Service
5285 Port Royal Road
Springfield, VA 22161
703-605-6000

Table of Contents

1 Executive Summary

Since the launch of the Soil Moisture Active Passive (SMAP) satellite mission in 2015, post-launch calibration and validation (Cal/Val) activities have been guided by two primary objectives: 1) To calibrate, verify, and improve the performance of the science algorithms; and 2) to validate the accuracy of the science data products as specified in the SMAP Level 1 mission science requirements. This report provides an assessment of the latest, Version 7 (V7) SMAP Level 4 Carbon (L4_C) product. The L4_C global record now spans eight years (March 2015 – present) of SMAP science operations, including seven major reprocessing updates to the operational product. These updates include various L4_C algorithm refinements and calibration adjustments to account for changes in ancillary inputs.

The SMAP L4_C algorithm estimates a global, daily terrestrial carbon budget that is informed by daily surface and root-zone soil moisture information from the SMAP Level 4 Soil Moisture (L4_SM) product and by land cover from the Moderate Resolution Imaging Spectroradiometer (MODIS), canopy fractional photosynthetic active radiation (fPAR) from the Visible Infrared Imaging Radiometer Suite (VIIRS), and other ancillary biophysical data. The L4_C product provides estimates of global, daily net ecosystem CO_2 exchange (NEE) and the component carbon fluxes, namely, vegetation gross primary production (GPP) and soil heterotrophic respiration (R_H). Other L4_C product elements include surface (ca. 0-5 cm depth) soil organic carbon (SOC) stocks and associated environmental constraints, including soil moisture-related controls on GPP and R_H ecosystem respiration (Kimball, Jones, and Glassy 2014; Jones et al. 2017). The L4_C product addresses SMAP carbon cycle science objectives by: 1) Providing a direct link between terrestrial carbon fluxes and underlying freeze/thaw and soil moisture-related constraints; 2) Documenting primary connections between terrestrial water, energy and carbon cycles; and 3) Improving understanding of terrestrial carbon sink activity.

L4_C is calibrated against eddy covariance (EC) tower CO_2 flux measurements, which are a proxy for terrestrial ecosystem NEE. The L4_C product has self-imposed performance requirements related to NEE, the primary product field for validation, although the other L4_C product fields (namely GPP, R_H, and SOC) have demonstrated utility for carbon science applications (Liu et al. 2019; Endsley et al. 2020; Wurster et al. 2021). The L4_C targeted accuracy requirement is to stay below a mean unbiased root-mean-square (RMS) error (ubRMSE, or standard deviation of the error) for NEE of 1.6 g C m^{-2} d^{-1} (or, equivalently, 30 g C m^{-2} yr^{-1}), emphasizing northern (≥45°N) boreal and arctic ecosystems; this accuracy is similar to that of EC tower CO_2 flux observations (Baldocchi 2008). The methods used for L4_C performance and validation assessment have been established from the SMAP Cal/Val plan and previous studies (Jones et al. 2017; Endsley et al. 2020) and are reported here for L4_C V7.

Our primary validation compares L4_C V7 estimates of NEE, GPP, and ecosystem respiration (RECO) to EC tower flux measurements at 26 globally distributed SMAP Core Validation Sites. We also compared the L4_C V7 mean annual fluxes, interannual variability, and short-term trends to the recent literature and to independent reference datasets, including: solar-induced fluorescence data from the Orbiting Carbon Observatory-2 mission; global, up-scaled EC tower fluxes from an ensemble of machine-learning models; global soil carbon inventory records; an ensemble of dynamic global vegetation models; and two indices of recent (2015-2022) climate oscillations.

V7 shows a slight, statistically insignificant increase in RMSE compared to the previous version, largely owing to the unavoidable change from MODIS to VIIRS fPAR inputs. The L4_C product continues to exceed the target NEE accuracy and continues to show favorable accuracy for GPP and RECO. GPP and RECO interannual variability also show good agreement with independent estimates, particularly in the northern hemisphere. A comparison of recent L4_C flux variability with the literature and with El Niño Southern Oscillation indices demonstrates that L4_C can represent the response of the terrestrial carbon-cycle to moisture and temperature variability, particularly in southern, semi-arid regions. Similarly, L4_C surface SOC anomalies in the southern hemisphere show variability that closely corresponds to recent drying and re-wetting trends.

These assessments underscore the utility of L4_C for diverse science applications; indeed, L4_C surface SOC was recently used in a NASA DEVELOP project, sponsored by Conservation International, for assessing the spatial and temporal variability of irrecoverable carbon reserves (Noon et al. 2021) in Peru and Bolivia. Other recent examples include the use of L4_C for constraining the magnitude and timing of the northern hemisphere land carbon sink (Endsley et al. 2022; Watts et al. 2023); estimating the impact of the COVID-19 pandemic on global carbon emissions (Ray et al. 2022); evaluating the impact of changes to a land surface model (Huang et al. 2022); diagnosing the response of ecosystem productivity to extreme climatic events, including droughts, heatwaves, and ice storms (Li and Wei 2020; Kwon et al. 2021; Dannenberg et al. 2022; Yang and Liu 2023); and regional monitoring of cropland conditions for projecting annual crop yields (Wurster et al. 2021).

2 Version 7 Algorithm and Product Updates

The updates in the L4_C Version 7 (V7) algorithm address changes made to the L4_SM drivers as part of L4_SM V7. These include changes to L4_SM estimates of root-zone soil moisture, surface soil moisture, and surface soil temperature, which are used to drive the operational L4_C V7 product. In addition to these changes, L4_C V7 was recalibrated using the L4_SM Nature Run version 10 (NRv10), a multi-decadal simulation using the L4_SM V7 land modeling system that is not informed by SMAP brightness temperature retrievals. Model spin-up to the soil-organic carbon equilibrium state was also changed in V7. While the L4_SM Nature Run climatology (2000-Present) was previously used in L4_C spin-up, in V7 we instead used the L4_SM ensemble Open Loop (2015-Present) climatology to minimize the difference in climatology between the L4_C spin-up and forward operations. No changes were made to the core L4_C algorithm.

Another major change in L4_C V7 is the adoption of a new fraction of photosynthetically active radiation (fPAR) dataset, which is used as a key model input for estimating vegetation productivity. In all prior versions of L4_C, fPAR data were obtained from the Terra MODIS MOD15A2H product. However, as the Terra satellite is nearing the end of its mission (Endsley et al. 2023), it has become imperative to switch to a new source of fPAR data with global coverage, favorable performance, and low latency matching those of the MODIS heritage record. The Visible Infrared Imaging Radiometer Suite (VIIRS) sensors aboard the Suomi NPP (SNPP), NOAA-20 and NOAA-21 satellites are similar to the MODIS sensors aboard Terra and Aqua, and a VIIRS VNP15A2H fPAR product is already available. Therefore, L4_C V7 is the first L4_C product version using VIIRS fPAR data. Prior to recalibration, we applied a bias correction, using cumulative distribution function (CDF) matching, to our MODIS Collection 6.1 fPAR data so as to better match VIIRS Collection 1 fPAR at eddy covariance (EC) tower sites. This is necessary because most of our EC tower flux data were collected prior to the launch of SNPP VIIRS. The operational L4_C V7 product is run exclusively using the VIIRS VNP15A2H Collection 1 product as the sole fPAR input.

We recalibrated the L4_C model Biome Properties Look-up Table (BPLUT) by optimizing L4_C predicted GPP and RECO fluxes against observed GPP and RECO fluxes from a global network of 356 EC flux towers (Pastorello et al. 2020; Ukkola et al. 2021). New calibration software was used in L4_C V7; the major difference is that an open-source re-implementation of Sequential Least-Squares Quadratic Programming (Kraft 1994; Johnson 2023) was used instead of the default, closed-source implementation in Matlab. As in the previous L4_C Version 6 (V6) calibration, in V7 soil litter decay rates were again adjusted to improve L4_C agreement with independent datasets in the initial size of soil organic carbon (SOC) stocks. Following recalibration of the BPLUT, the L4_C initial SOC pool sizes were initialized as described by Jones et al. (2017), based on an updated L4_SM soil moisture and temperature climatology.

3 L4_C Product Performance

The L4_C V7 product continues to perform within specified accuracy requirements (Jones et al. 2017), with unbiased root-mean squared error (ubRMSE) in mean daily NEE well below 1.6 g C m^{-2} day^{-1} (Figure 1). Relative to the previous Version (V6) product, when compared to observed fluxes at the Core Validation Sites, the V7 product shows stable performance albeit with a slight, statistically insignificant increase in RMSE and decrease in spatial correlations (Figure 2) for NEE, GPP, and RECO. Viewed over the entire, 8-year L4_C production record, however, NEE ubRMSE has generally improved with each new product version (Figure 3).

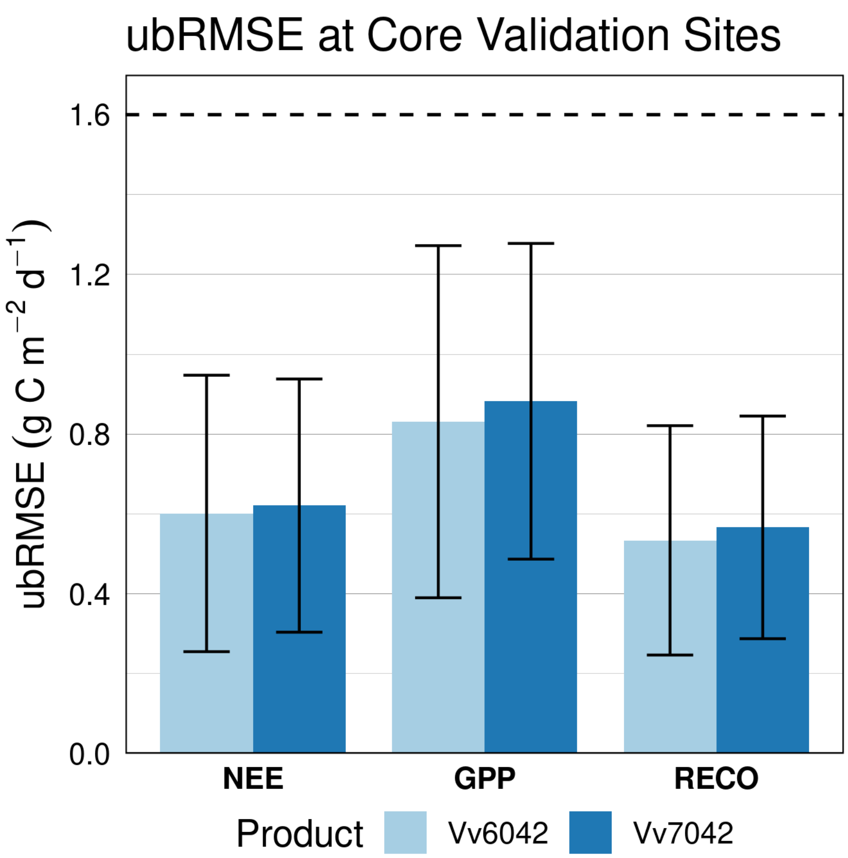

Figure 1: Unbiased root-mean squared error (ubRMSE) against observations at eddy covariance (EC) flux towers, averaged for the entire set of 26 SMAP Core Validation Sites, for net ecosystem exchange (NEE), gross primary productivity (GPP), and total ecosystem respiration (RECO). Metrics are shown for the L4_C V6 and V7 products with Science Version Identifiers Vv6042 and Vv7042, respectively.

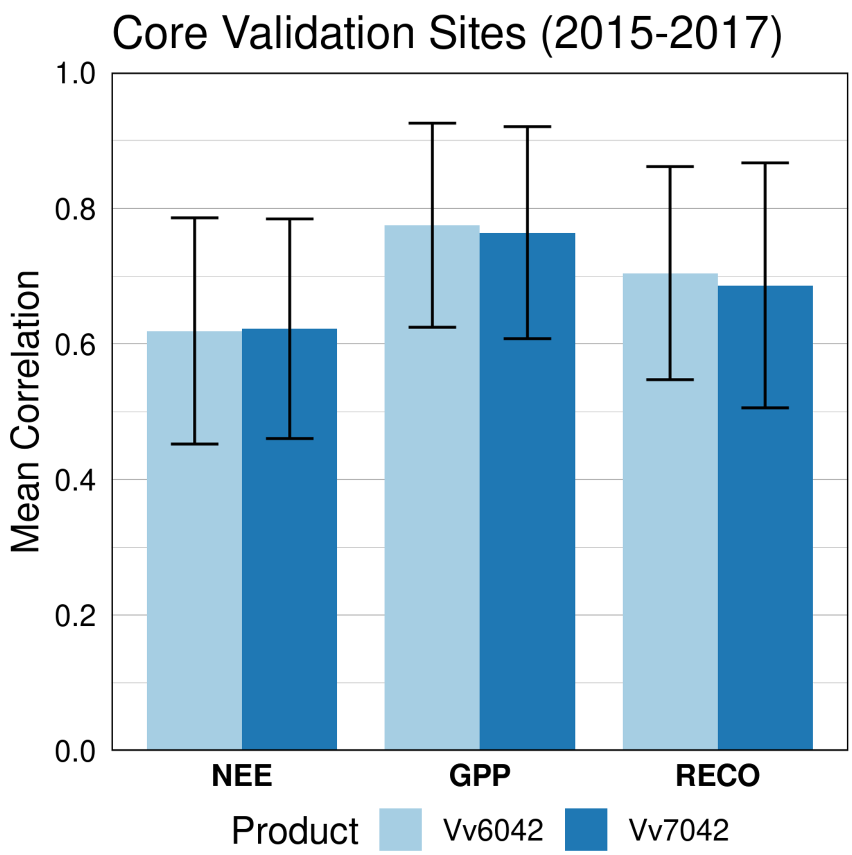

Figure 2: As in Figure 1 but for the time series correlation coefficient.

We attempted to attribute the change in skill between V6 and V7 for L4_C component fluxes by analyzing the covariation in the change in RMSE (ΔRMSE) and the change in the relevant input driver data. This analysis was performed by pooling data from all tower Core Validation Sites on all available days. For GPP, ΔRMSE may be a function of change in vegetation fPAR (from MODIS fPAR in V6 to VIIRS fPAR in V7), change in L4_SM root-zone soil moisture (SMRZ), or change in the parameterization of the GPP response to SMRZ. For RECO, ΔRMSE may be a function of change in L4_SM soil temperature (T_{soil}), L4_SM surface soil moisture (SMSF), or the parameterization of the R_H response to either of these.

The 20th and 80th percentiles of ΔRMSE were used as indicators of significant changes in predictive skill (worst increases in RMSE and best decreases in RMSE, respectively). Site-days where GPP skill improved in V7 have higher root-zone soil moisture than in V6 and show little to no change in fPAR between product versions; a decline in GPP skill in V7 is associated with large changes in fPAR as well as drier root-zone soil moisture (not shown).

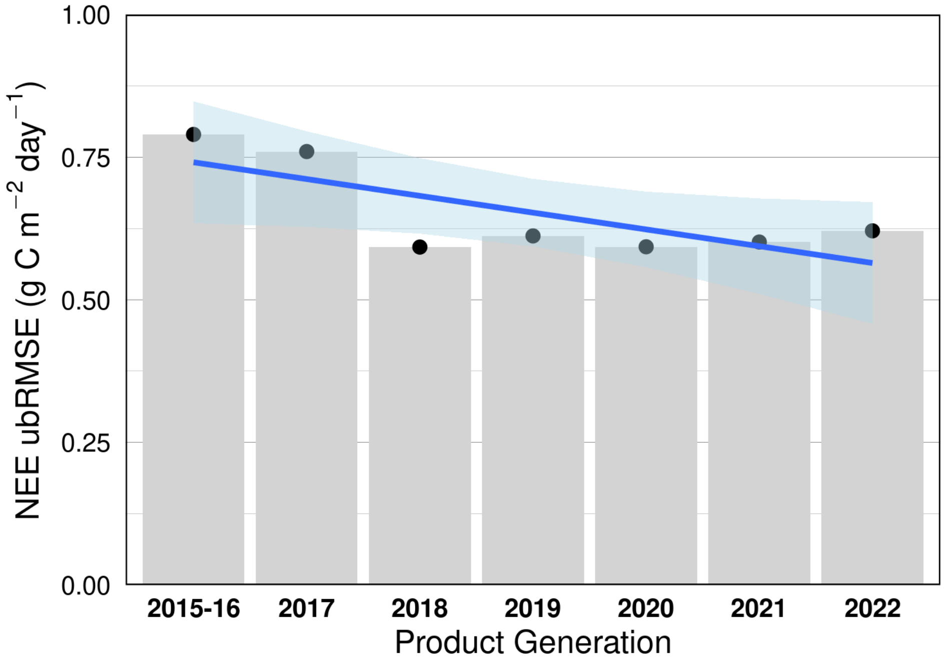

Figure 3: Unbiased root-mean squared error (ubRMSE) in NEE against 2015-2017 observations at SMAP Core Validation Sites for each product version by release year, beginning with the initial Version 1 "beta" release in 2015-16. Product generations 2021 and 2022 correspond to L4_C V6 and V7, respectively. For each version, the validation period is April 2015 through December 2017; ubRMSE for versions prior to 2018 have been re-validated against the 2015-2017 dataset, for consistency.

The decline in GPP skill is partly due to the change from MODIS fPAR to VIIRS fPAR (not shown); the latter data are known to have different quality assurance (QA) flagging for clouds and aerosols (Yan et al. 2021), and the afternoon overpass of SNPP VIIRS leads to significantly different fPAR retrievals in the tropics (Xu et al. 2018). For optical remote sensing of vegetation conditions in humid or tropical regions, the morning overpass of Terra MODIS is preferable (Tang et al. 2020), and we expect that lower-quality fPAR retrievals in these regions lead to lower-quality GPP estimates. As seen in Figure 4a, VIIRS fPAR shows early saturation at high values in most of the tropics (20 S through 10 N); lower latitudes are also areas where GPP differs the most between V6 and V7 GPP (Figure 4b).

The change in GPP skill is also partly due to a change in the E_{mult} constraint, which may reflect changes in SMRZ, the re-calibrated parameters related to SMRZ, or both (not shown). While site-days with higher GPP RMSE in V7 are often drier than in V6, they almost exclusively show higher E_{mult} values as well, suggesting V7 SMRZ parameters should be re-examined (not shown). In particular, the increased GPP RMSE on drier site-days in V7 is consistent with the reduced sensitivity to SMRZ at higher SMRZ values for deciduous broadleaf and cropland areas (not shown).

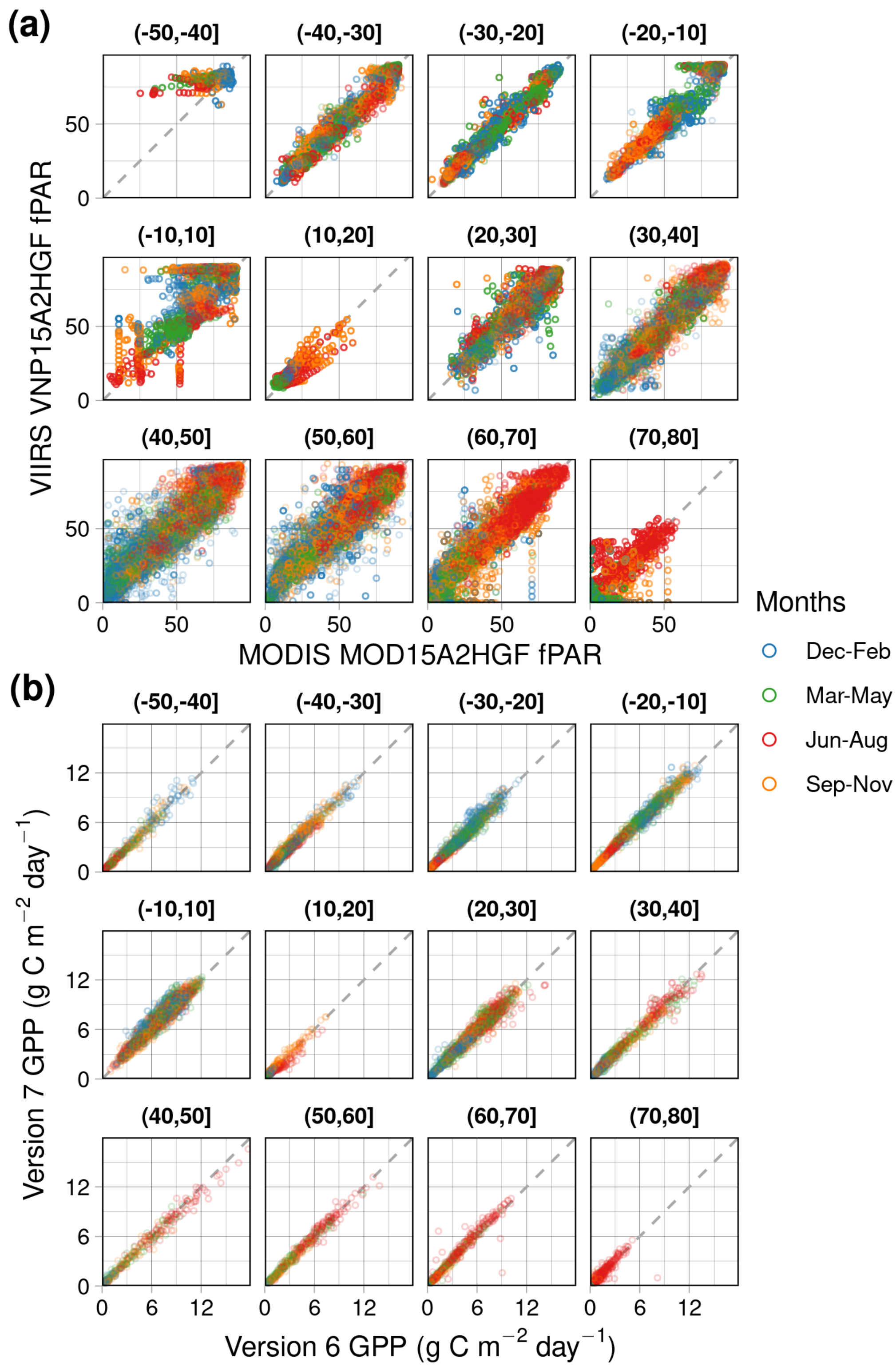

Figure 4: Comparison plots of (a) MODIS and VIIRS fPAR (percent units) and (b) L4_C V6 and V7 GPP, at FLUXNET sites, broken out by season (color-coded symbols). Subplots show results for 12 latitude bands between 50 degrees S latitude (-50) and 80 degrees N latitude; dashed line denotes 1:1 line.

Examining RECO ΔRMSE, we found that site-days with the greatest increase in RECO RMSE between V6 and V7 are generally warmer and drier (not shown). RECO sensitivity to surface soil moisture generally *increased* in V7. Site-days where RECO RMSE increased most show the greatest changes in both L4_SM SMSF and L4_SM T_{soil} between versions; site-days with RECO improvement are associated with virtually no change in the L4_SM data. However, both the best and the worst site-days in V7 show a similar pattern of change in the W_{mult} constraint. We conclude that while the T_{soil} parameterization in L4_C V7 could likely be improved, part of the increase in RECO RMSE is due to upstream changes in L4_SM SMSF.

4 Calibration and Climate Differences from Prior Release

Model calibration (via non-linear optimization) using updated L4_SM and fPAR driver datasets results in changes to the ancillary BPLUT (Figure 5). Maximum light-use efficiency (ε_{max}) increased for woody plant functional types (PFTs) other than deciduous needleleaf forest (DNF) but decreased for cropland types. This pattern of change can be seen in a map of global changes in mean annual GPP (Figure 6); most of the L4_C land domain shows an increase in mean annual GPP between product versions, but there are notable decreases in global croplands, particularly in Europe, Northeast China, and Central India.

Changes to the SMRZ and vapor pressure deficit (VPD) constraints on GPP are more complicated than changes to ε_{max}. They can be evaluated in terms of whether the linear ramp function became more or less steep between product versions. An increase in the ramp function's slope is characterized by a minimum bound that increases and a maximum bound that decreases between V6 and V7 (Figure 5); a decrease in the slope is characterized by the opposite changes. An increased slope represents stronger sensitivity but over a narrower *range.* The *range* of sensitivity of GPP to VPD (Max_{VPD} minus Min_{VPD}), as one example, increased significantly for DNF, but this also means that similar changes in VPD produce less of a response in DNF GPP. Croplands and deciduous broadleaf forest (DBF) have higher, narrower sensitivity to SMRZ in V7 than in V6.

The general increase in the BPLUT parameter Max_{SM} (Figure 5) indicates that the SMSF constraint on R_H was slightly relaxed (lower sensitivity over broader range) in V7 compared to V6. R_H declined slightly in tropical and southern temperate evergreen broadleaf forests (EBF) but increased elsewhere, compared to the previous version. R_H strongly increased in high-northern latitude shrublands (≥55 N; Figure 7), despite a slight decrease in the decay rate (K_{mx}) because the temperature sensitivity of R_H in shrublands (SHB) increased (Figure 5). This translates into lower surface SOC storage in V7 in this region (Figure 8).

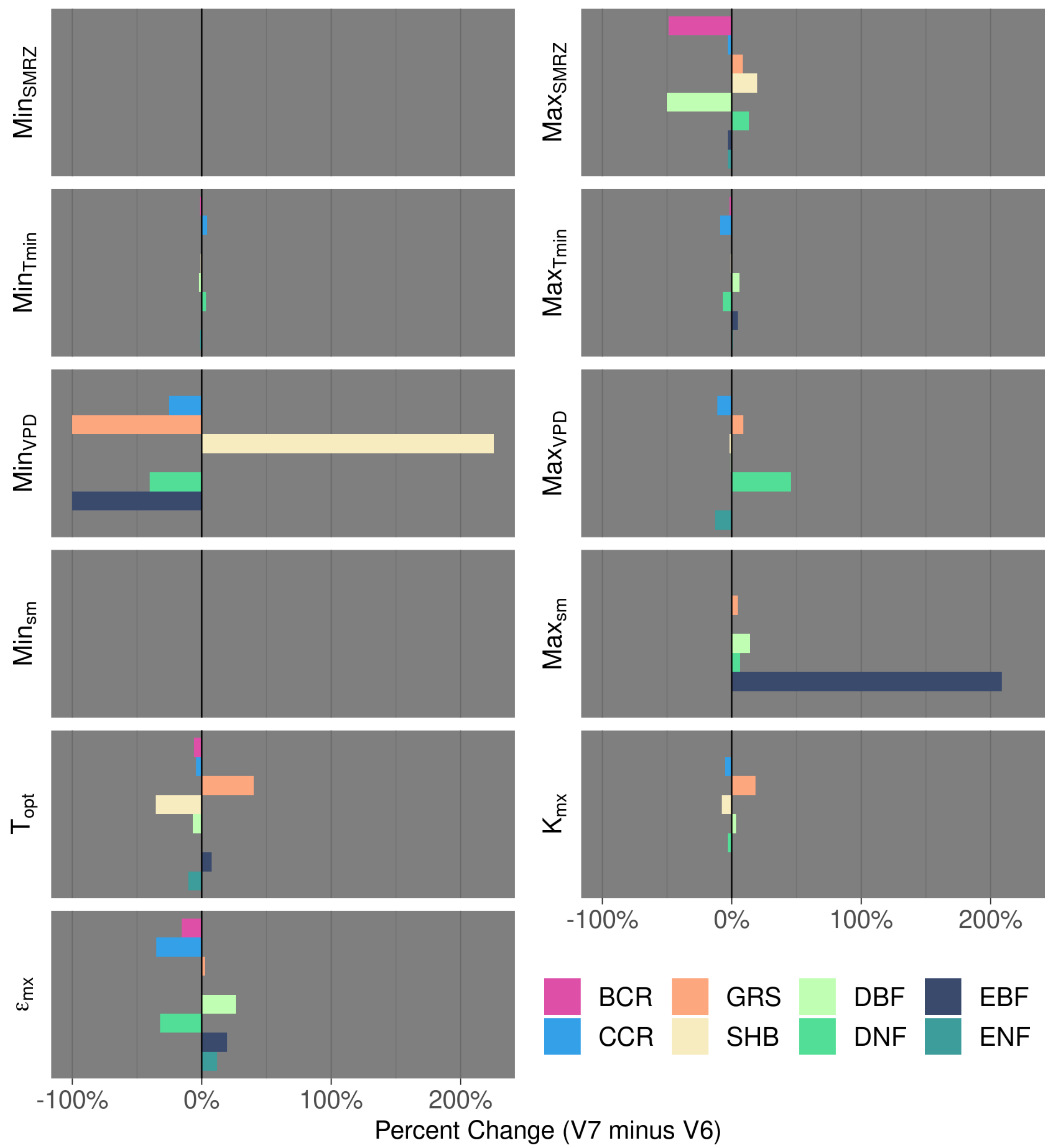

Figure 5: Percent change in BPLUT parameters from V6 to V7. Descriptions of parameters can be found in Kimball et al. (2014, their Table 5). The abbreviations "ENF" through "BCR" refer to, respectively: Evergreen Needleaf, Evergreen Broadleaf, Deciduous Needleleaf, Deciduous Broadleaf, Shrublands, Grasslands, Cereal Croplands, and Broadleaf Croplands.

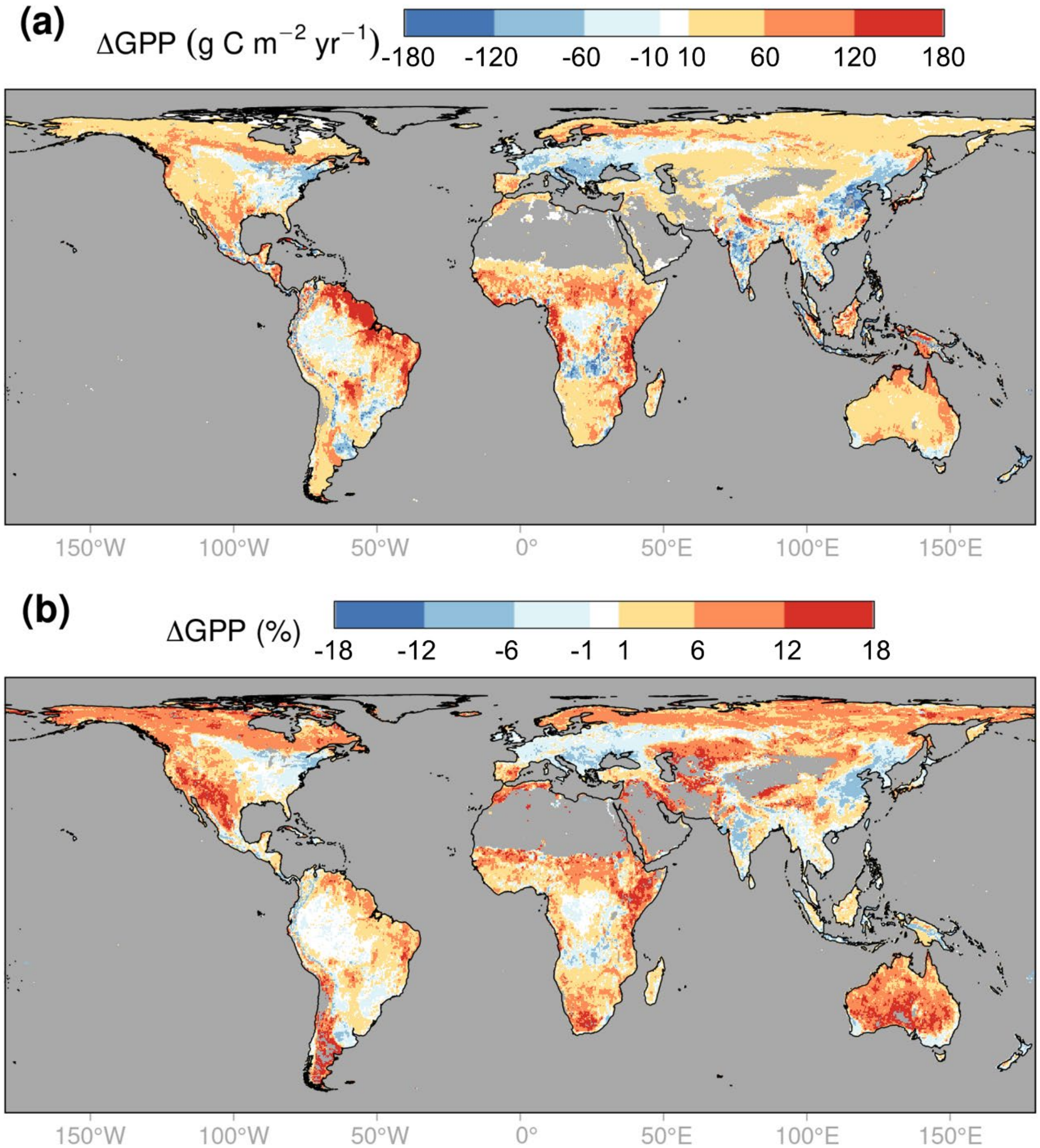

Figure 6: V7 minus V6 difference in mean annual gross primary productivity (GPP) for 2016-2019 in (a) absolute and (b) relative carbon flux terms. Relative fluxes are in terms of percentage of mean annual flux. Positive (red) values indicate greater GPP in V7 than in V6.

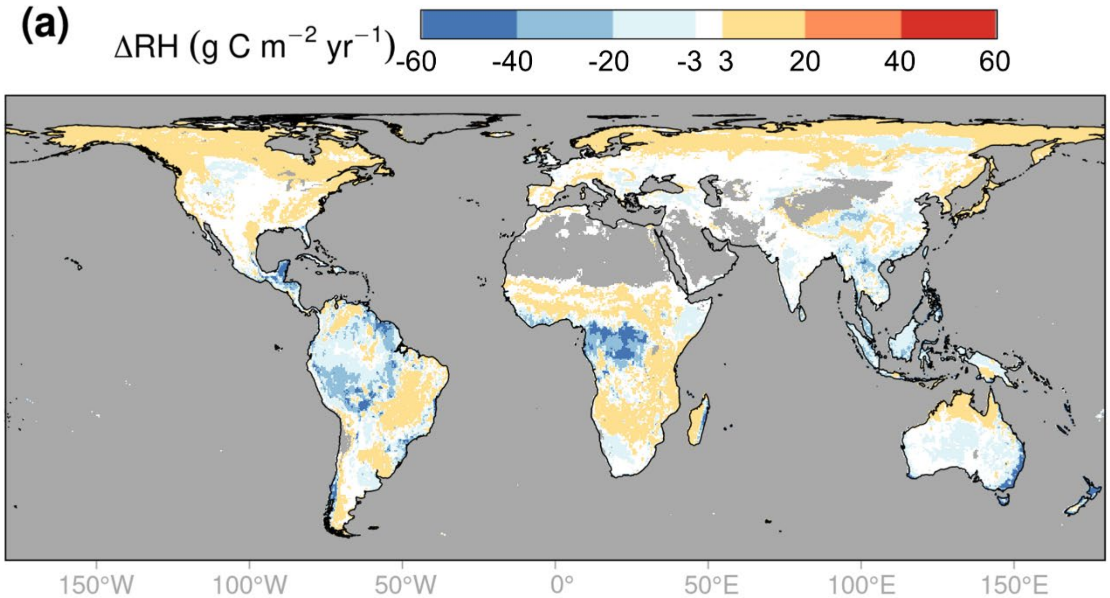

Figure 7: As in Figure 5 but for heterotrophic respiration (R_H). Positive (red) values indicate greater R_H in V7 than in V6.

Calibration against tower fluxes resulted in a larger value of T_{opt} in grasslands (GRS; Figure 5) and thus a narrowing of the range of the temperature sensitivity of R_H (see equation 11 of Kimball et al. 2014). But the predicted SOC distribution in this land-cover type was still higher than expected, so we manually adjusted K_{mx}, decreasing the turnover time. Despite these changes, there were no significant differences in annual R_H flux or SOC magnitudes. Comparing L4_C SOC from both product versions (V6 and V7) with independent reference data from SoilGrids (v1) 250m surface layer (0-5 cm) SOC storage (Hengl et al. 2017), we find that GRS SOC storage is closer to the SoilGrids estimate in V7 than in V6 whereas SHB SOC has diverged further (not shown). There is still a large under-estimate of SOC storage above 60 N latitude (Figure 8). See Section 5.2 for further discussion.

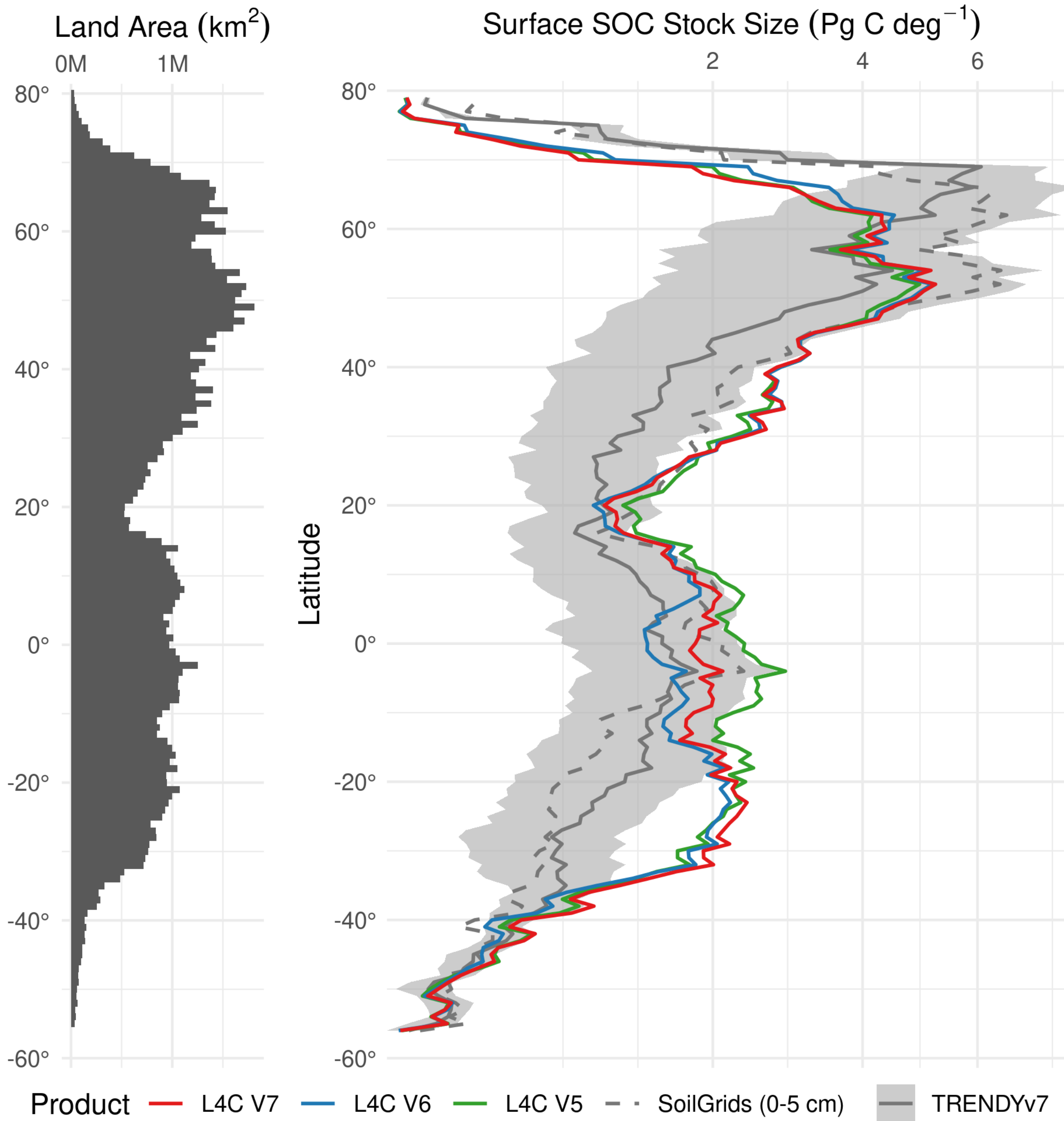

Figure 8: (Right) Latitude-band summary of surface soil organic carbon (SOC) storage in multiple products, including the three most recent L4_C versions (V5, V6 and V7), the SoilGrids 250m product's top 5-cm layer, and the TRENDYv7 ensemble mean and spread. The ensemble mean from TRENDYv7, which is expected to represent the top 1 meter of soil, has been interpolated to match the top 5-cm estimate of L4_C (Endsley et al. 2020). (Left) Latitudinal distribution of L4_C land area (km^2).

4.1 Global Peatlands

In L4_SM V7, soil moisture and soil temperature data are informed by a reassessment of the global distribution of, and soil porosity in, peatlands, which impacts L4_C V7 carbon flux and SOC estimates. Areas designated as peatlands in the new L4_SM product have greater soil porosity than in the previous version. This results in potentially significant changes in soil moisture (and, to a lesser degree, soil temperature) inputs in V7 compared to V6. *A priori,* it is expected that peatlands would be generally wetter and cooler than predominantly mineral soils when situated in otherwise similar climate conditions. However, because of their higher soil porosity in V7, peatlands in L4_C may be modeled as having stronger water limitations on R_H and GPP than other soils, given the potentially lower relative saturation because, to first order, the same amount of water input from precipitation has more volume to fill.

We compared L4_C V7 fluxes to L4_C V6 fluxes in high northern-latitude (≥50 N) peatlands at FLUXNET tower sites for each calendar month (not shown). Tower NEE observations indicate that peatland towers (N=21) have lower seasonal NEE amplitudes than non-peatland towers (N=83) above 50 N latitude. L4_C generally reproduces this pattern, except that the differences between peatland and non-peatland towers are much smaller and L4_C predicts a summer-time CO_2 sink at peatland towers of equal or greater magnitude than non-peatland towers. When comparing V7 to V6, we find that the seasonal NEE cycle has a larger amplitude in V7 than in V6, and that the summertime CO_2 sink strength is enhanced in July and August.

We also compared L4_C V7 fluxes and environmental constraints in peatlands to those of non-peatlands for all pixels in the high-northern (≥50 N) EASE-Grid 2.0 land domain, where peatlands are defined by L4_SM land pixels with an increase in porosity between V6 and V7 (Figure 9). In contrast to both the observed and simulated NEE at FLUXNET sites, monthly NEE distributions for all northern land pixels show larger seasonal-cycle amplitudes in peatlands than in non-peatlands; i.e., peatlands are predicted to be a greater CO_2 source in winter and a greater CO_2 sink in summer than non-peatlands. The greatest difference between peatlands and non-peatlands in V7 occurs during May, when peatlands are a significantly greater CO_2 sink than non-peatlands. This difference is much less pronounced in summer and there is no difference between peatlands and non-peatlands NEE in late summer and fall. This summertime sink activity is enhanced in V7 relative to V6, which otherwise displays the same pattern.

Differences in NEE between northern peatlands and non-peatlands can be partly understood in terms of the R_H flux. During the winter, peatlands are a slightly stronger source of CO_2 to the atmosphere (i.e., more positive NEE) than non-peatlands (Figure 9) due to a greater R_H flux. This greater, mean R_H flux in northern peatlands is mostly a result of warmer peatland soil temperatures rather than of wetter soils, which are largely frozen during the northern winter. As winter progresses in northern latitudes, peatland soil temperatures decline more slowly than in non-peatlands and in some years may display short-term increases associated with warmer weather (not shown), likely because of the higher heat capacity associated with the higher water content in peatlands.

In northern spring, however, soil temperatures in non-peatlands increase faster and eventually overtake mean soil temperatures in peatlands. This results in a faster rise in non-peatland R_H fluxes. In summary, northern peatlands have smaller amplitudes in the seasonal cycle of soil temperatures, compared to non-peatlands. The higher thermal inertia of peatlands causes them to become a stronger C source in winter and a stronger C sink in spring (Figure 9). By mid-to-late summer, mean peatland NEE is largely consistent with that of non-peatlands. When we compare the monthly NEE flux distributions (peatlands versus non-peatlands) in V7 to that of V6 (not shown), we find that these patterns are enhanced in V7 (lower seasonal-cycle amplitudes in peatlands in V7 than in V6), indicating that the upstream changes to L4_SM in peatlands have helped to differentiate respiration processes in northern peatlands. As peatlands have higher monthly E_{mult} than non-peatlands throughout the year (not shown), we can infer that the particular difference in spring sink activity in peatlands is due to suppressed R_H flux at that time, rather than enhanced GPP flux.

5 Independent Assessments

The L4_C carbon budget can be compared to similar estimates from terrestrial biosphere models, Dynamic Global Vegetation Models (DGVMs), and statistical upscaling models. In particular, we might ask how L4_C estimates compare to independent products in terms of the mean carbon (CO_2) flux, its interannual variability, and trend. Here, we compared the L4_C V7 record with similar carbon flux estimates from other global reference data and assessments.

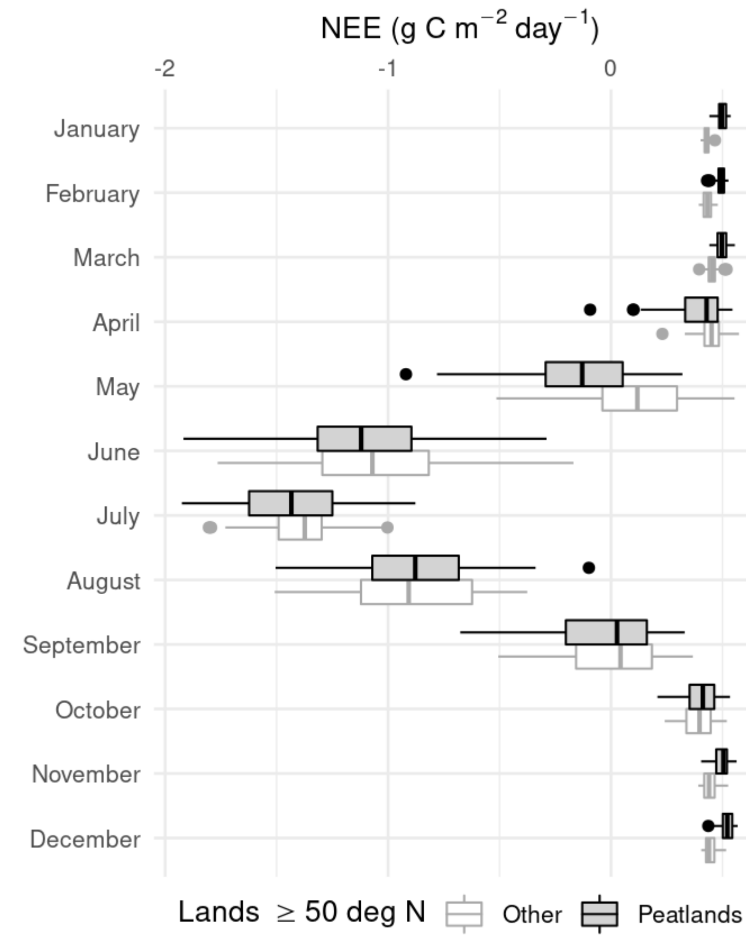

Figure 9: Monthly mean L4_C (V7) net ecosystem exchange (NEE) in all northern peatlands versus all other (non-peatland) northern lands. Peatlands are defined as those areas where the L4_SM land model's total soil porosity increased between V6 and V7, which reflects the incorporation of a new peatlands map in V7 of this upstream product.

5.1 Global Carbon Budget

The mean global GPP flux estimated by L4_C V7, for the period 2016-2022, is 131.4±2 Pg C $year^{-1}$. Based on an informal literature review (Table 1), the L4_C estimate is close to the average annual GPP flux (128.9 Pg C $year^{-1}$) estimated from 33 studies since about 2003. These studies span multiple time periods, however, and there are several factors that could induce a trend in the global annual GPP (or NPP) flux (Zhao and Zeng 2014; Mao et al. 2016; Peñuelas et al. 2017; Chen et al. 2019). A recent validation of the latest MODIS MOD17 global productivity record arrived at a similar mean annual flux (for 2012-2021) of 130.0±1.5 Pg C $year^{-1}$ (Endsley et al. 2023). The same study found that this value agrees well with the TRENDYv7 DGVM ensemble mean (128.6±1.4 Pg C $year^{-1}$) for the same period.

Table 1: Mean global GPP flux estimated in multiple studies, for different periods of assessment, based on an informal review of the literature. The period of assessment is denoted with "n.a." when it could not be determined from the study. See the bibliography for each complete reference.

Publication	Total GPP (Pg C year^{-1})	Period
Ruimy et al. (1996)	133.0	n.a.
Still et al. (2003)	150.0	n.a.
Alton et al. (2007)	126.0	n.a.
Sasai et al. (2007)	131.5	2001-2004
Demarty et al. (2007)	129.0	n.a.
Joiner et al. (2008)	140.8	2007
Yuan et al. (2010)	110.0	2000-2003
Beer et al. (2010)	123.0	1998-2005
Ryu et al. (2011)	118.0	2001-2003
Jung et al. (2011)	119.0	1982-2008
Chen et al. (2012)	132.0	2003
Koffi et al. (2012)	146.0	n.a.
Mao et al. (2012)	146.3	2000-2009
Piao et al. (2013)	133.0	n.a.
Parazoo et al. (2014)	127.4	2010
Cai et al. (2014)	119.4	n.a.
Yan et al. (2015)	128.2	n.a.
Yebra et al. (2015)	107.0	2000-2011
Harper et al. (2016)	128.0	2016
Zhang et al. (2016)	129.3	2007-2015
Zhang et al. (2016)	134.2	2000-2007
Wei & Yi (2017)	107.5	2001-2005
Madani et al. (2018)	134.2	1950-2000
Yu et al. (2018)	112.0	2004-2012
Norton et al. (2019)	166.7	2015
Li & Xiao (2019)	135.5	2000-2017
Badgley et al. (2019)	147.0	n.a.
Zheng et al. (2020)	106.2	1982-2017
Tagesson et al. (2020)	121.8	1982-2015
Madani et al. (2020)	130.0	1982-2016
Wang et al. (2021)	128.3	1982-2019
Bi et al. (2022)	125.0	1992-2020
Zhang et al. (2023)	129.7	2001-2018
AVERAGE ± Std Dev.	**128.9 ± 13**	n.a.

The mean annual NPP flux (2016-2022) estimated in L4_C V7 is 79.6±1.3 Pg C year^{-1}. This is higher than the inter-model spread of the TRENDYv7 DGVM ensemble and about 20 Pg C year^{-1} higher than the ensemble median (Endsley et al. 2023). In L4_C, NPP is a fixed fraction of autotrophic C uptake (GPP). This fraction (the NPP:GPP ratio or plant carbon-use efficiency, CUE), with values ranging from 0.47 (Evergreen Broadleaf) to 0.79 (Deciduous Broadleaf), is higher in V7 than the oft-cited multi-biome mean of ~0.5 (DeLucia et al. 2007). A recent synthesis study suggests that the global mean NPP:GPP ratio is closer to 0.46 but varies widely, between 0.22 and 0.79 (Collalti and Prentice 2019). It is this range, [0.22, 0.79] that was used as the prior bounds on the NPP:GPP ratio during calibration of L4_C; that values are pushed to the higher end of this range suggests a model bias that cannot be overcome by the cost function when calibrating against tower fluxes. Our experience with L4_C, and the evidence that GPP is not itself overestimated (see above), suggests that the problem is a high bias in R_H, which leads to a low bias in autotrophic respiration, R_A (R_A being the difference between GPP and NPP). The L4_C V7 mean annual R_H flux (2016-2022) is 78.6±0.9 Pg C year^{-1}, which is also higher than other independent estimates for recent periods (Zaehle 2013; Konings et al. 2019).

Finally, L4_C V7 estimates a global NEE land sink (2016-2019 average) of 2.3±0.9 Pg C year^{-1}, which is of comparable magnitude, though lower, than the Global Carbon Budget's estimate for 2015-2019 of 3.3±0.5 Pg C year^{-1} (Friedlingstein et al. 2020). It is also lower than the estimated 2010-2019 mean (3.7±0.5 Pg C year^{-1}) from the Global Carbon Assimilation System, version 2 (GCASv2), which is based on satellite observations of atmospheric CO_2 concentration (Jiang et al. 2022). NOAA's CarbonTracker (Jacobson et al. 2023) estimates a mean land C sink of 2.7 Pg C year^{-1} for 2015-2020 (compare to Global Carbon Budget) and 3.2 Pg C year^{-1} for 2010-2019 (compare to GCASv2).

The global NEE flux estimated by L4_C V7 in each year is calculated as the difference between RECO and NPP; as a difference calculation, it is highly sensitive to small changes in NPP and RECO. In 2016, the earliest complete year available, L4_C V7 estimates an unusually strong land C sink of -3.8 Pg C year^{-1}, approximately twice as large as subsequent years and more than twice as large as the mean 2015-2016 sink estimated from the Orbiting Carbon Observatory-2 (OCO-2) satellite mission (Crowell et al. 2019). As the estimated 2016 R_H flux is quite average, this strong, negative annual NEE appears to be due to an above-average annual GPP flux (141.4 Pg C year^{-1}) in 2016 (Figure 10). Breaking this flux out by TransCom region (Baker et al. 2006), the 2016 GPP flux can be attributed to high GPP flux in northern mid-latitude regions: Europe, Eurasia Temperate, and North American Temperate regions, in particular (not shown).

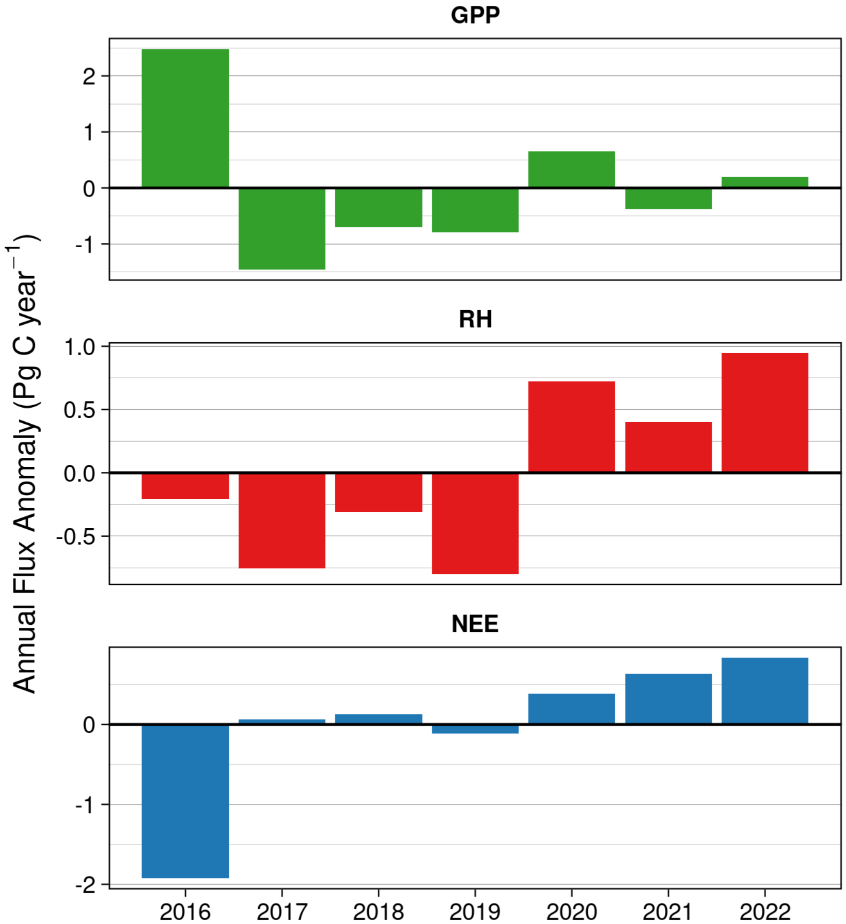

Figure 10: Anomalies in the annual, global flux modeled in L4_C V7, by year.

Mapping annual NEE fluxes indicates that, while the northern hemisphere land C sink usually shows high spatial heterogeneity, in 2016 most northern lands were synchronized in strong sink activity (Figure 11). It has been suggested that a strong northern-hemisphere land C sink may account for the recovery of the global net land sink following the 2015-2016 El Niño (Wigneron et al. 2020). L4_C V7, within this short period of record (2015-2022) that includes only one major El Niño phase, displays a stronger global land C sink during El Niño (see Section 6, "Global Teleconnections"), which is consistent with more recent studies (Hu et al. 2019; Cai et al. 2020; Du et al. 2021) and suggests that increased moisture in some water-limited ecosystems and increased canopy-intercepted solar radiation in the tropics could contribute to the stronger land C sink in 2016.

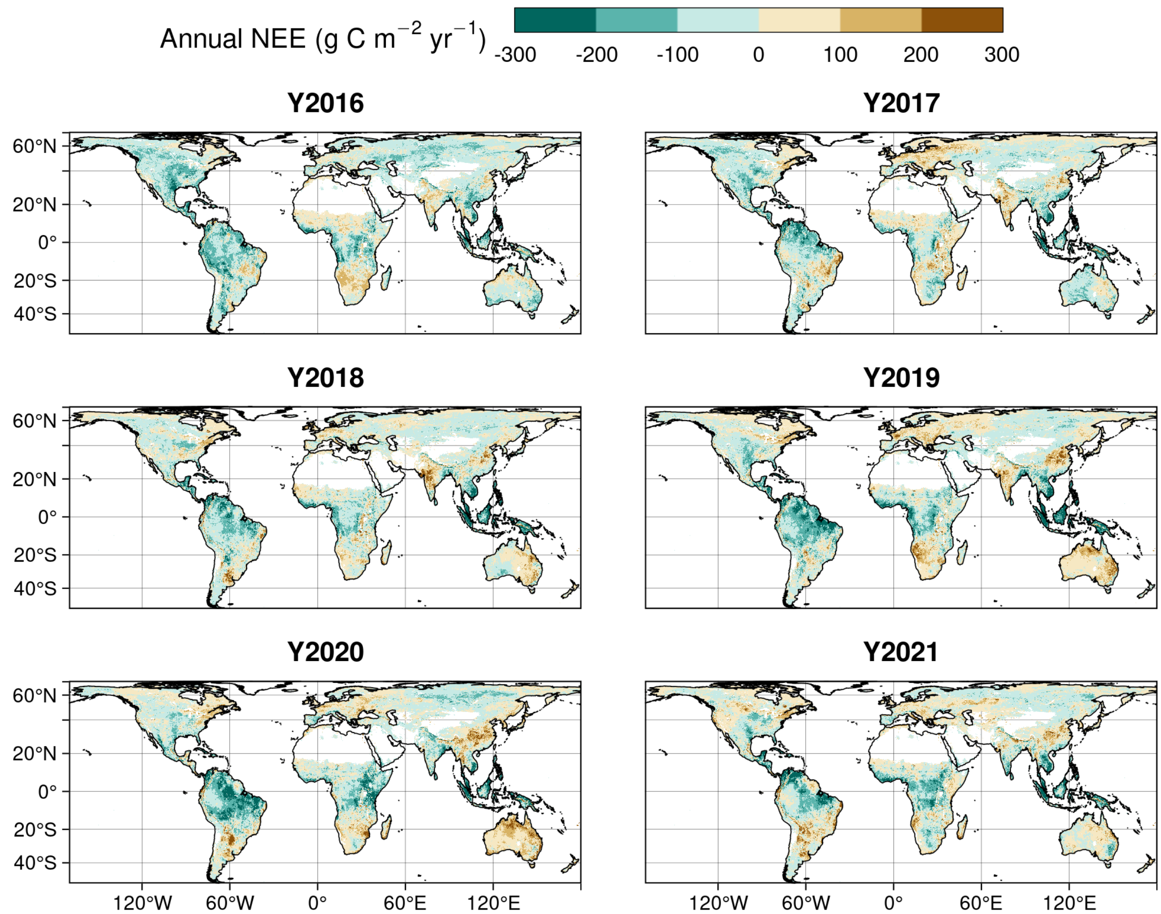

Figure 11: Annual NEE flux per year in L4_C V7. Global L4_C NEE maps were resampled to 36 km prior to plotting.

5.2 Mean Surface Soil Organic Carbon Stock

Surface (0-5 cm) SOC content is the amount of soil C supporting the modeled R_H flux from this most labile soil layer. We can compare L4_C surface SOC to similar estimates from other models. The TRENDYv7 DGVM ensemble includes an estimate of total soil column SOC content; using global soil profiles derived from SoilGrids 250m, the TRENDYv7 estimates can be scaled to produce an SOC estimate for the top 5 cm soil layer, similar to L4_C surface SOC (Endsley et al. 2020). As depicted in Figure 8, L4_C V7 reproduces the global surface SOC storage magnitudes seen in similar products and in the previous version of L4_C. In the tropics and extra-tropical northern latitudes, L4_C surface SOC closely matches the SoilGrids 250m estimate and is either within or close to the range of estimates from the TRENDYv7 ensemble of DGVMs.

Systematic biases that have persisted through multiple product versions are still evident, however: Boreal and tundra SOC storage (≥50 N latitude) is under-estimated while southern temperate (below 20 deg S latitude) SOC storage is over-estimated. The latter is likely a consequence of the southern extratropics being dominated by two PFTs, SHB and GRS, that are found throughout the L4_C global land domain and in varying climates. In model calibration, we regress to the mean. This results in overestimated SHB and GRS SOC storage in the southern extratropics but underestimated SOC storage for these same PFTs in the boreal and tundra regions, relative to SoilGrids. The global FLUXNET tower network is also particularly sparse in the southern extratropics (Schimel et al. 2015), which imposes a regional limitation on model calibration and validation.

5.3 Mean and Interannual Variability

We compared L4_C monthly total GPP and RECO fluxes to those of two ensemble estimates of terrestrial carbon fluxes: the TRENDYv7 ensemble mean's "S3" simulation, which includes varying atmospheric CO_2, climate, and land use; and the FLUXCOM RS+METEO ensemble (hereinafter referred to simply as FLUXCOM) of statistical learning models trained on FLUXNET data. TRENDYv7 mean monthly GPP displays a phase shift to earlier in the year (not shown), relative to L4_C, though L4_C's estimate of the seasonal cycle is likely accurate, given that it is constrained by satellite observations of vegetation cover. Indeed, the L4_C GPP seasonal cycle aligns well with that of FLUXCOM across most TransCom regions (Figure 12). TRENDYv7 and L4_C show very similar magnitudes of GPP in the northern hemisphere but a strong phase shift in the southern hemisphere, where L4_C GPP can be more than 50 g C m^{-2} $month^{-1}$ higher than the TRENDYv7 estimate. L4_C GPP is also higher than the FLUXCOM estimates for the southern hemisphere (Figure 12).

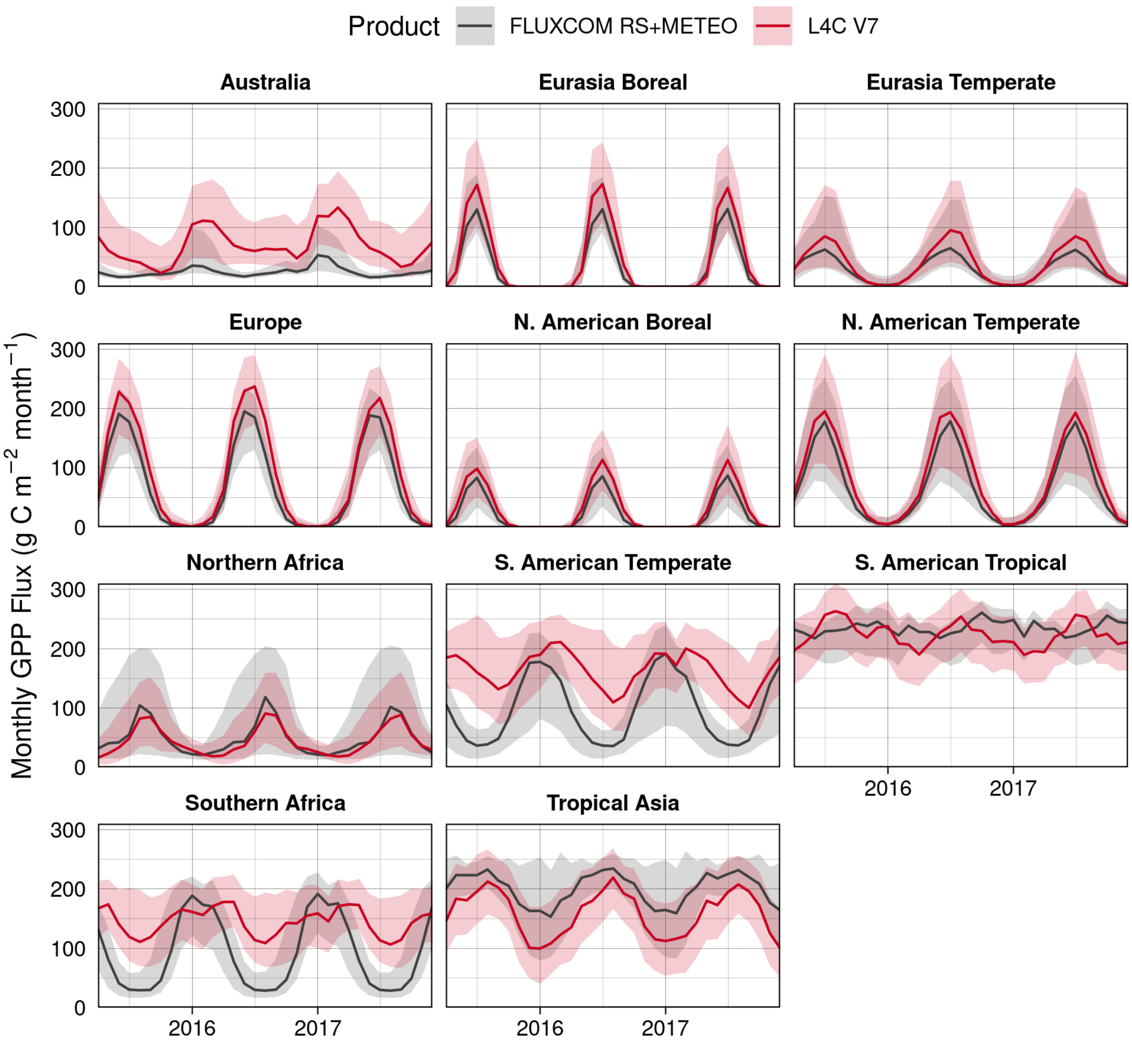

Figure 12: Monthly GPP flux from (red) L4_C V7 and (black) the data-driven, upscaled FLUXCOM RS+METEO product averaged over TransCom regions. Shaded regions show the interquartile range (range between 25th and 75th percentiles) among pixels in each region.

Similarly, L4_C GPP shows excellent agreement with satellite-based solar-induced chlorophyll fluorescence (SIF, mW m^{-2} nm^{-1} sr^{-1}) derived from the OCO-2 mission (Figure 13), where SIF is a byproduct of photosynthesis and an observational proxy for GPP (Joiner et al. 2014). Global, spatially contiguous SIF (CSIF) data based on OCO-2 retrievals, available at 0.05-degree resolution on 4-day intervals (Zhang et al. 2018), were resampled onto the global 9-km EASE-Grid 2.0, summarized by TransCom region, and converted to Z-scores for the SMAP post-launch period through the end of 2019. For most of the global land domain, L4_C GPP is strongly correlated with SIF (Pearson's $r \geq 0.84$). The apparent smoothness of the CSIF time series, compared to that of L4_C, is likely due to multiple factors: the CSIF data have been subjected to greater spatial and temporal aggregation; they are derived from a neural network trained on aggregated

OCO-2 SIF retrievals under cloud-free conditions and informed by 16-day MODIS nadir bi-directional reflectance distribution-adjusted reflectance (NBAR) composites; and “a gap-filling and smoothing algorithm” (Zhang et al. 2018) is applied to the MODIS NBAR data.

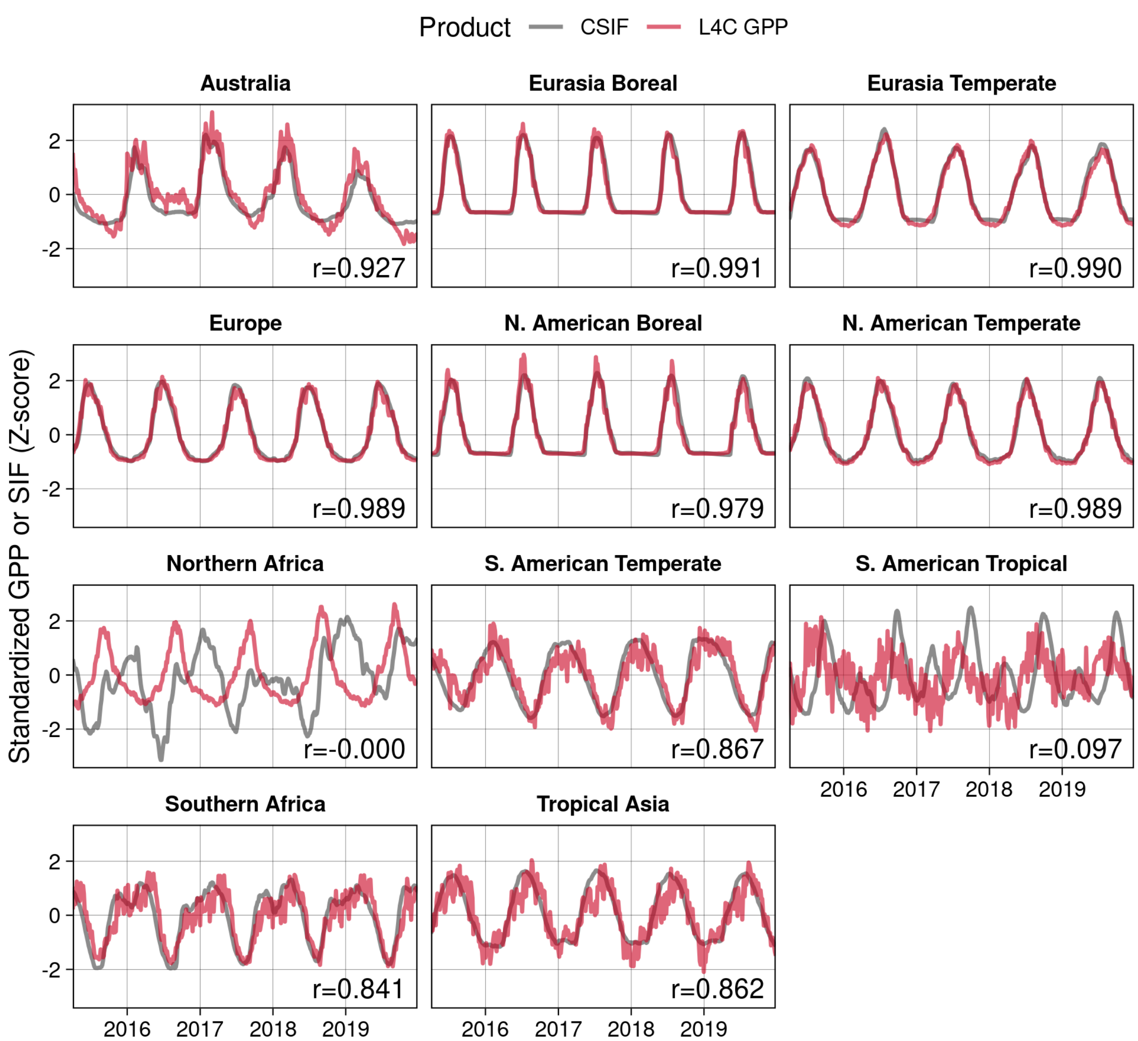

Figure 13: 4-day Z-scores of contiguous solar-induced chlorophyll fluorescence (CSIF) and L4_C GPP, summarized by TransCom region, with Pearson’s correlation coefficients indicated at top-right.

However, in two regions, L4_C GPP fails to match the productivity time series seen in the SIF data. In the South American Tropical region (Figure 13), SIF shows a biannual cycle of productivity; L4_C only reproduces the larger peak in productivity and with an approximate 3-month lag. This is likely a reflection of the weak seasonality of satellite-based fPAR in this region. In Northern Africa, L4_C predicts a very different seasonal pattern than indicated from the SIF observations. However, both SIF and L4_C GPP show a distinct increasing productivity trend in this region, which is consistent with previous satellite vegetation and field biomass studies (Leroux et al. 2017; Anchang et al. 2019).

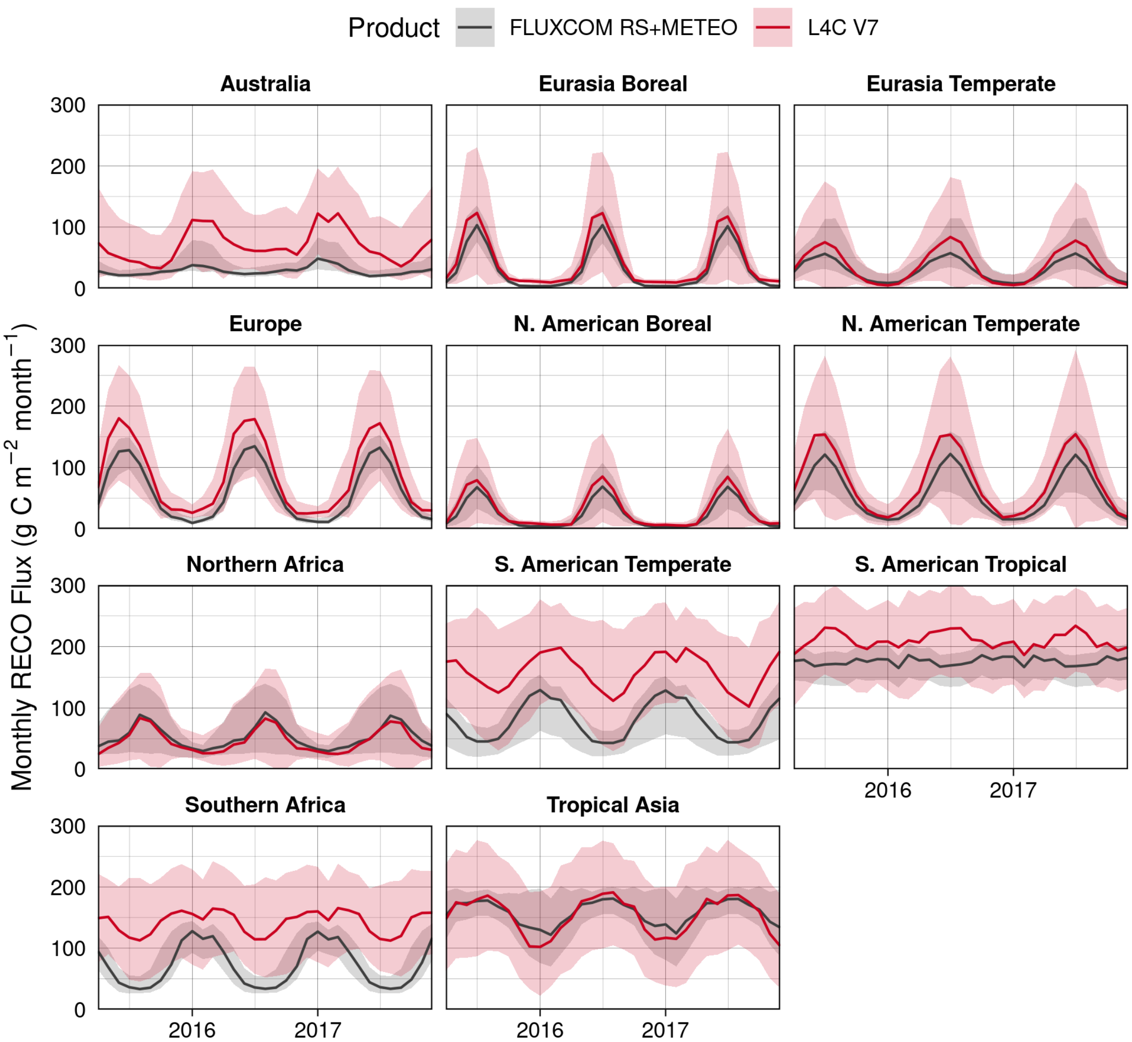

Figure 14: As in Figure 12 but for RECO.

We also compared L4_C V7 ecosystem respiration (RECO) to FLUXCOM and both R_H and RECO to TRENDYv7. The L4_C RECO seasonal cycle matches that of FLUXCOM at monthly time scales though L4_C RECO has much higher spatial variability than FLUXCOM (Figure 14). L4_C RECO is also generally higher than FLUXCOM RECO, except in Tropical Asia. L4_C R_H shows a phase shift toward later in the year in some regions, relative to TRENDYv7, at monthly time scales (not shown). Again, L4_C R_H is a better match with TRENDYv7 in the northern hemisphere, though the amplitude of the R_H seasonal cycle is high, relative to TRENDYv7, in most regions (not shown).

Monthly NEE was calculated from FLUXCOM RECO and GPP data as RECO minus GPP. L4_C V7 NEE shows a slight phase shift toward later in the year at the monthly scale, relative to FLUXCOM (Figure 15), which is similar to the reported phase shift in L4_C V6 daily NEE (Endsley et al. 2022). However, L4_C NEE is a good match for the seasonal NEE amplitude in the northern hemisphere. In the southern extratropics, FLUXCOM predicts a stronger seasonal cycle, and greater magnitude, of the land carbon sink than L4_C V7.

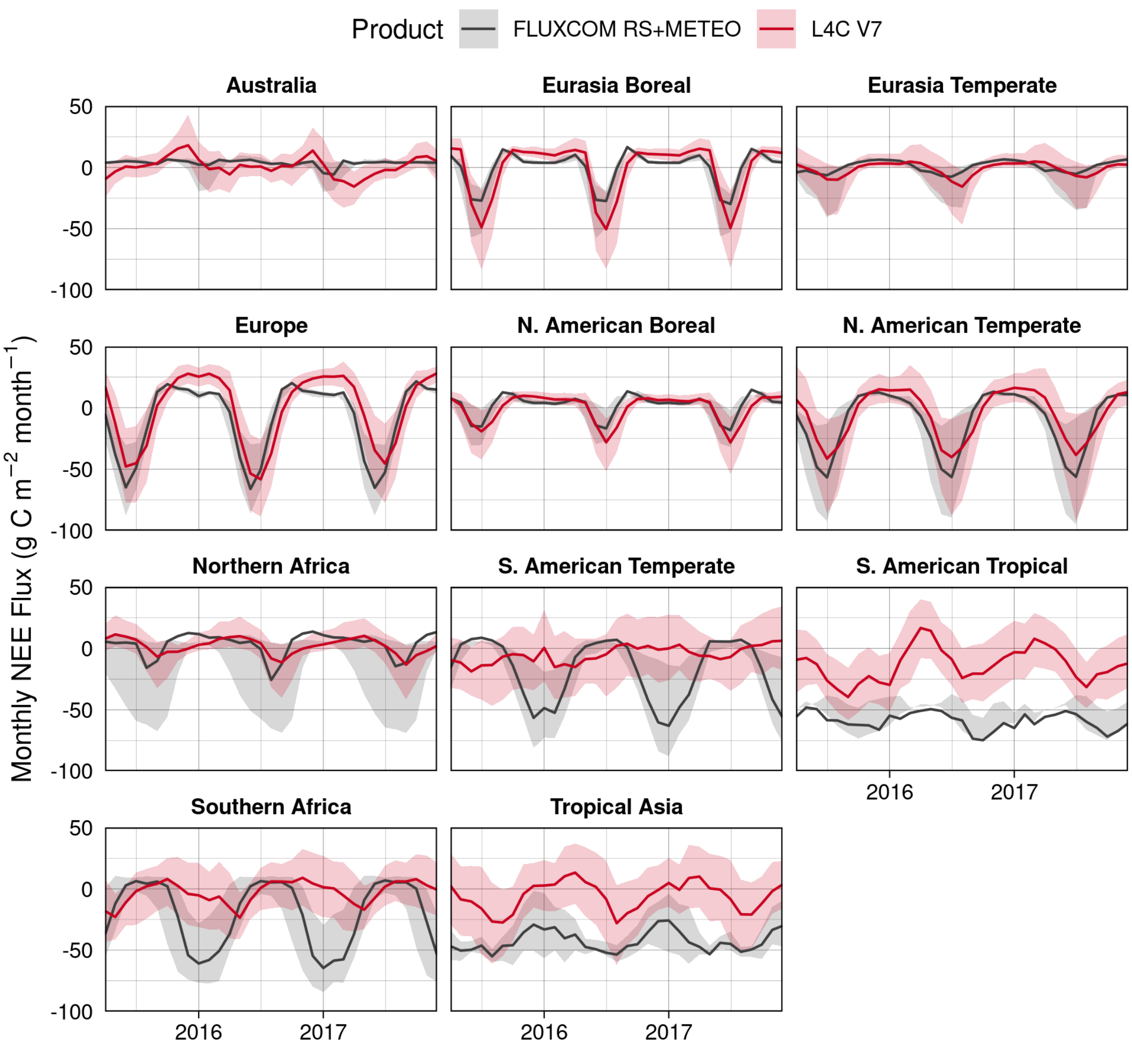

Figure 15: As in Figure 12 but for NEE.

Using the methodology of Ahlström et al. (2015), we computed the relative contribution of different regions to the interannual variability of fluxes in L4_C V7. South America and Southern Africa contribute approximately 43% of the global interannual variability in GPP in L4_C V7, and Tropical Asia and Australia contribute an additional, combined 8%. This is consistent with reports about the significance of seasonal moisture variability in the semi-arid tropics (Poulter et al. 2014; Ahlström et al. 2015). South America and Southern Africa also contribute 33% of the global interannual variability in R_H in L4_C V7. Despite the importance of these regions to both land CO_2

uptake (GPP) and soil CO_2 losses (R_H), however, these regions contribute little to the global interannual variability in NEE in L4_C V7, which is dominated by contributions from northern temperate regions that are inconsistent between years. This suggests that modeled GPP and R_H fluxes are incorrectly timed or biased in L4_C V7, as multiple lines of evidence point to the importance of southern, semi-arid regions to the land sink interannual variability (Piao et al. 2020).

5.4 Variability in Surface Soil Organic Carbon

A distinguishing factor of the L4_C product is that it provides what is likely the only global, daily, satellite-based estimates of surface SOC content. While SOC stocks do indeed vary on sub-annual time scales (Cagnarini et al. 2019; Padarian et al. 2022), there is no established method for validating dynamic SOC estimates. Field-based estimates of SOC content are destructive, which prevents longitudinal assessment of change in SOC stocks. However, modeled changes in SOC, such as those provided by L4_C, can be correlated with known climatic variation. A time series of surface SOC residuals from L4_C V7, with the seasonal cycle and long-term trend removed, reveals interesting interannual variation that corresponds well with short-term climatic variation (Figure 16). While northern-hemisphere regions exhibit little systematic variation, southern-hemisphere regions show a strong response to the 2015-2016 El Niño, which brought warm and dry conditions that likely suppressed soil decomposition and the R_H flux, leading to a build-up of surface SOC stocks of between 2-4% of their 2015 magnitudes. More recently, persistent La Niña conditions seem to have reversed this trend, with surface SOC stocks returning to their 2015 values. In Australia, 2019 was both the warmest and driest year in that country's record and it was followed, in 2020, with above-average rainfall commencing immediately in January 2020 (Australia Bureau of Meteorology 2021). This pattern of climate variability likely explains the sharp increase in surface SOC stocks followed by rapid SOC loss at the beginning of 2020.

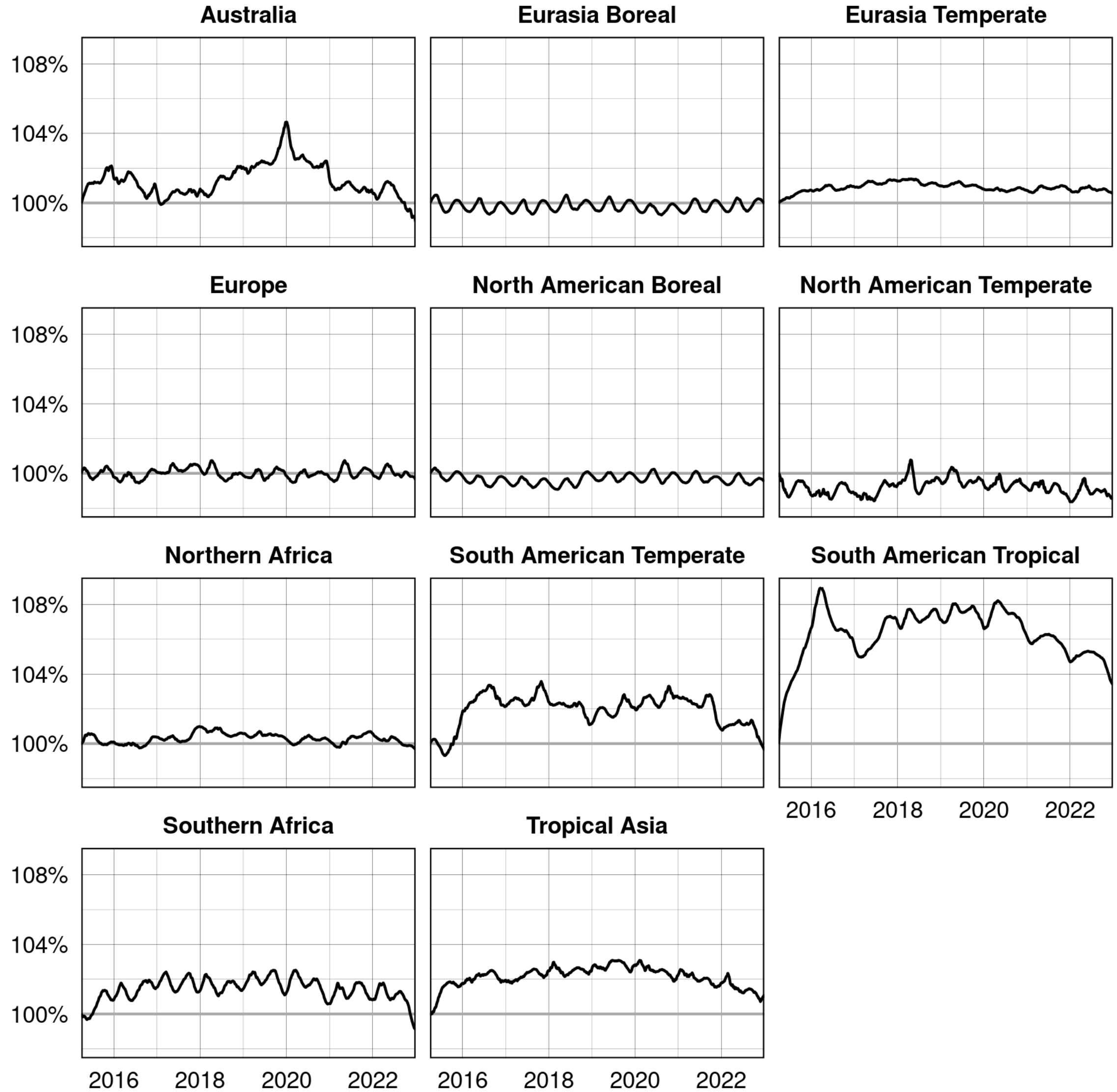

Figure 16: Detrended residuals from a harmonic regression of regional surface SOC stocks, shown for select TransCom regions; the seasonal cycle and long-term trend are removed. Residuals are added to the initial March 31, 2015) surface SOC stock size and expressed as a percentage of the initial stock size. The regular oscillations seen in the subplots for regions with low (e.g., Southern Africa) or essentially no residual SOC change (e.g., North American Boreal) are an artifact of harmonic regression.

5.5 Recent Trends

While the L4_C record (2015-present) is not yet long enough for statistically robust trends to be inferred, examining the trends apparent in L4_C V7 can provide an indication as to how climate trends captured in the L4_C meteorological inputs are driving carbon fluxes. Based on harmonic regression of daily total fluxes, at global extent, L4_C V7 displays a significant (p-value<0.001), upward trend in NEE (diminishing global land CO_2 sink strength) of 1.3 Tg C year^{-2} (not shown). This appears to be explained by increasing ecosystem respiration (0.9 Tg C year^{-2}, p-value<0.001), mostly due to increasing R_H (1.0 Tg C year^{-2}, p-value<0.001), which is consistent with previous reports based on field data (Bond-Lamberty et al. 2018; Lei et al. 2021). Naidu and Bagchi (2021) recently suggested that upward trends in NPP (demonstrated elsewhere) are not sufficient to counter-balance rising soil R_H.

L4_C V7 displays insignificant (p-value>0.1), weak negative trends in GPP and NPP over 2015-2022 (not shown). However, these trends, as well as the trends in other fluxes, are affected by the strong response of the modeled carbon cycle to the 2015-2016 El Niño (Figure 11). If data from 2015-2016 are discarded, we find upward trends in all fluxes, including GPP and NPP, with RECO increasing fastest. These upward trends across the modeled carbon budget are consistent with reports of an increase in the seasonal amplitude of the terrestrial carbon sink (Forkel et al. 2016; He et al. 2022). Broken out by TransCom region, we find divergent trends in GPP, with significant (p-value <0.001), upward trends in southern temperate regions and significant (p-value <0.0002) downward trends in northern temperate regions (not shown). Similarly, northern temperate regions show a strong, upward trend (p-value <0.001) in NEE since 2017, with diminishing land sink amplitudes in recent years.

6 Global Teleconnections

L4_C fluxes respond to short-term climate variability (Jones et al. 2017; Wurster et al. 2021), particularly in global drylands, where rates of R_H are sensitive to SMAP-derived surface soil moisture estimates (Endsley et al. 2020). Regional and global climate oscillations, such as the El Niño Southern Oscillation (ENSO), should therefore influence the L4_C carbon budget through underlying model environmental constraints and be represented in the 8-year SMAP satellite record.

ENSO is a bimodal oscillation with two phases. The "warm" El Niño phase is associated with drought in the Amazon forest, Southern Africa, and Australia (Holmgren et al. 2001; Bastos et al. 2018) while the "cool" La Niña phase generally brings wetter conditions to these regions, and the associations are reversed in parts of the northern hemisphere (Zhang et al. 2019). A warm El Niño has also been associated with decreased GPP world-wide (Hashimoto et al. 2004; Zhu et al. 2017; Bastos et al. 2018) but particularly in the tropics, southern Africa, and Australia (Bastos et al. 2013); a cool La Niña phase is associated with a stronger land C sink, particularly in tropical drylands (Ahlström et al. 2015). Tropical ecosystem productivity is characterized by a response to warmer temperatures during El Niño and a response to higher precipitation during La Niña (Fang et al. 2017). Global atmospheric moisture patterns are also affected: warm-dry ENSO fluctuations are associated with higher VPD in the Amazon forest, Africa, and Australia but lower VPD in the southwest U.S., temperate South America, and parts of Siberia (Hashimoto et al. 2004). Similarly, Du et al. (2021) recently found associations between the El Niño phase and increased land surface wetness in the southwest U.S. and temperate South America; drier conditions associated with El Niño were found in the

Amazon forest, Southern Africa, southeast Asia, and much of Australia. Increased moisture associated with El Niño in North America is also consistent with a recent report by Hu et al. (2019) that this phase enhances the land C sink of this region. South America, which experiences the strongest direct effects of ENSO, generally receives less precipitation in the Amazon and more precipitation in the south, over Argentina, during a warm ENSO phase (Cai et al. 2020).

SOI and OLR, as measures of the bimodal ENSO oscillation, are negative during the El Niño phase and positive during the La Niña phase. We did not attempt to define a neutral phase in the SOI and OLR data, instead using all available monthly values in lagged correlations, allowing for up to a 3-month lag in SOI/OLR or L4_C. As both ENSO and terrestrial C fluxes are oscillating, Pearson's correlations between L4_C variables and SOI or OLR are best interpreted as "in-phase" (positive correlation) with ENSO or "out-of-phase" (negative correlation). As terrestrial ecosystems are generally more strongly affected by the warm-dry El Niño phase (Teckentrup et al. 2021), our discussion of ENSO associations emphasizes this phase. Seasonal associations are discussed in terms of the northern hemisphere (NH) summer or winter, for simplicity. We can separate these phases but the resulting estimates have reduced statistical power (56 months of La Niña conditions and 37 months of El Niño conditions during the 93-month assessment period, based on SOI).

We compared L4_C to two measures of ENSO fluctuations: the Southern Oscillation Index (SOI), compiled monthly by NOAA (2023), and the Outgoing Longwave Radiation (OLR) index (Chiodi and Harrison 2013). L4_C data included detrended, mean monthly L4_C NEE, GPP, R_H, and environmental constraint diagnostics: T_{mult}, W_{mult}, and E_{mult} which describe the normalized impact of T_{soil} on R_H, the normalized impact of SMSF on R_H, and the combined, normalized impact of minimum temperature, SMRZ, and VPD on GPP, respectively.

The L4_C environmental constraint diagnostics largely reproduce the aforementioned reported patterns. E_{mult} is associated with warm ENSO fluctuations in the Amazon, Southern Africa, Australia, and most of Tropical Asia; in these regions, warm ENSO fluctuations are associated with more limiting conditions for GPP, likely lower root-zone soil moisture or higher VPD (not shown). These correlations are generally weaker in the L4_C GPP data, except for Western Australia, which indicates strong ($r \approx 0.5$) declines in GPP with the onset of a warm El Niño (Figure 17). However, we do see weak out-of-phase correlations between GPP and ENSO throughout light-limited tropical forests, which may be explained by decreased cloud cover during El Niño leading to increased GPP despite drier conditions (Zhu et al. 2018). GPP in Southern Africa decreased strongly ($r \approx 0.6$) during the 2015-2016 El Niño, which included the driest precipitation period for the region in 35 years (Rembold et al. 2016); a similarly strong decline in Australia is associated with increased aridity (Bastos et al. 2018).

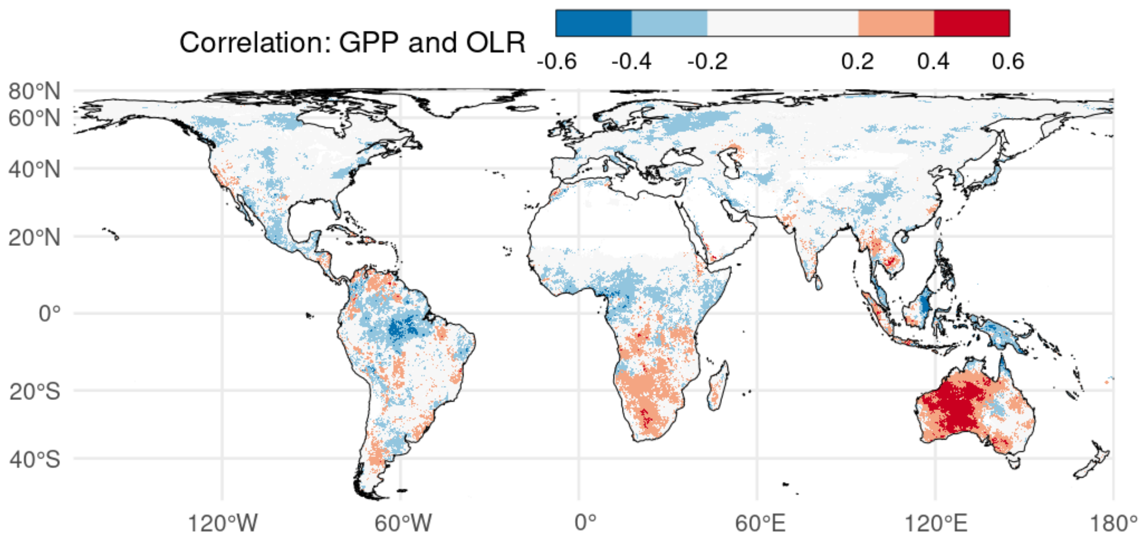

Figure 17: Time series correlation coefficient (2015-2022) between monthly, detrended L4_C GPP and the Outgoing Longwave Radiation (OLR) index, which is negative during the El Niño phase. Only significant (p-value≤0.05) correlations are shown (critical r ≈ ±0.2). Positive correlations (red) generally indicate decreased GPP during El Niño but possibly increased GPP during La Niña.

Significant, strong (r ≥0.5) correlations are found between SMSF and ENSO fluctuations throughout southeast Asia, indicating drier surface soils during El Niño (not shown). Warm ENSO fluctuations are associated with drier surface soil conditions across much of the global land domain, including the Amazon forest, Central Europe, Southern Africa, Australia, the North American Boreal forest, and parts of India and Central Asia. Conversely, cool ENSO fluctuations, such as the recent, multi-year La Niña phase, are associated with wetter surface soil conditions in Western North America and temperate South America.

The effect of ENSO on ephemeral T_{soil} appears to be dampened at monthly timescales, yet there are significant, moderate (r ≈ -0.4), negative correlations between T_{soil} and ENSO throughout the Andes of South America (not shown), which reflect warmer December-through-February near-surface air temperatures associated with El Niño (Cai et al. 2020). The OLR index shows stronger correlations than SOI with the T_{soil} environmental constraint (not shown).

These ENSO impacts on surface soils seem to induce periodic changes in soil decomposition, though the link is complicated by the positive response of R_H to both warmer (during El Niño) and wetter (during La Niña) conditions. The warm-dry El Niño phase is associated with decreased R_H in much of the southern hemisphere (Figure 18), but North America (by OLR and SOI) and India (by SOI only) show weak (r ≈ -0.25) negative correlations with ENSO, suggesting the opposite. The decline in tropical R_H associated with El Niño occurs mostly in during the NH winter months. The OLR index shows moderately strong (r ≈ 0.5) positive correlations with ENSO in the Amazon, Central Australia, and southeast Asia, indicating lower R_H during the warm El Niño phase. SOI correlations broken out by ENSO phase also suggest that R_H may increase in the Southeast U.S. and parts of Mexico during La Niña.

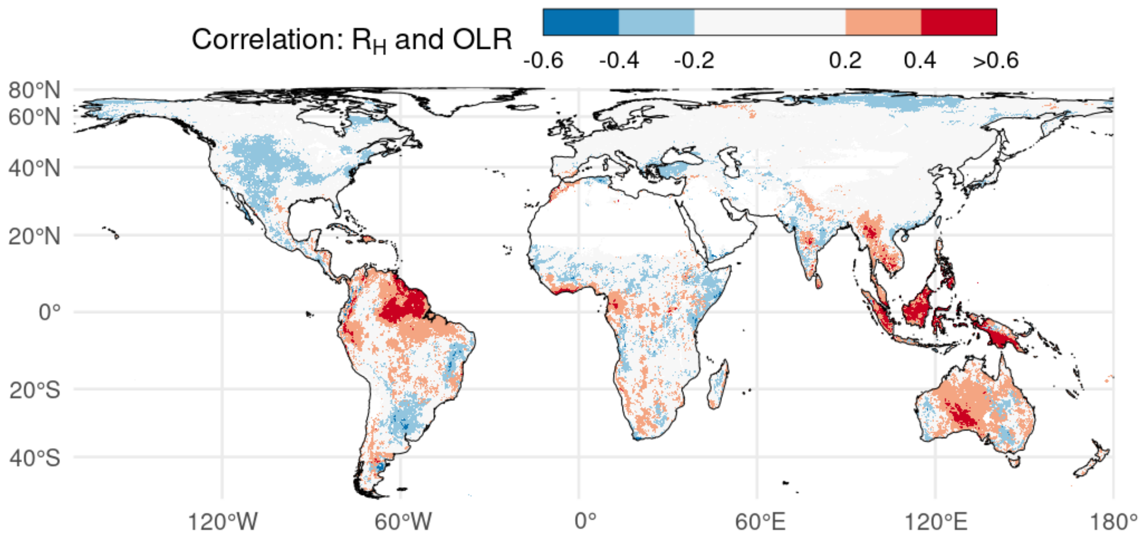

Figure 18: As in Figure 17 but for correlation between monthly, detrended L4_C R_H and the Outgoing Longwave Radiation (OLR) index. Positive correlations (red) generally indicate decreased R_H during El Niño but possibly increased R_H during La Niña.

Correlations between NEE and ENSO fluctuations are further complicated by the countervailing impacts of R_H and primary productivity, yet some generalizations can be made. In Southern Africa and most of Australia, NEE is weakly ($r \approx -0.3$) anti-correlated with ENSO (Figure 19), suggesting an enhanced land C sink during the cool-wet La Niña phase. Indeed, using an annual index of La Niña events (Chiodi and Harrison 2013, 2015), albeit a short record, we find annual L4_C NEE anomalies in Australia (and Tropical Asia) are strongly associated with La Niña (Figure 20).

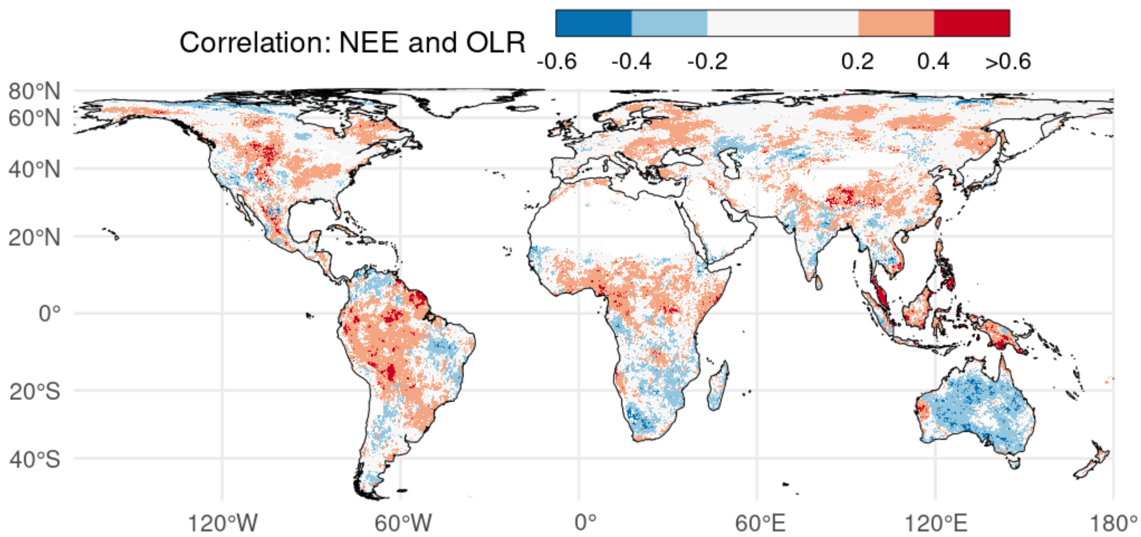

Figure 19: As in Figure 17 but for correlation between monthly, detrended L4_C NEE and the Outgoing Longwave Radiation (OLR) index. Positive correlations (red) generally indicate decreased NEE during El Niño but possibly increased NEE during La Niña.

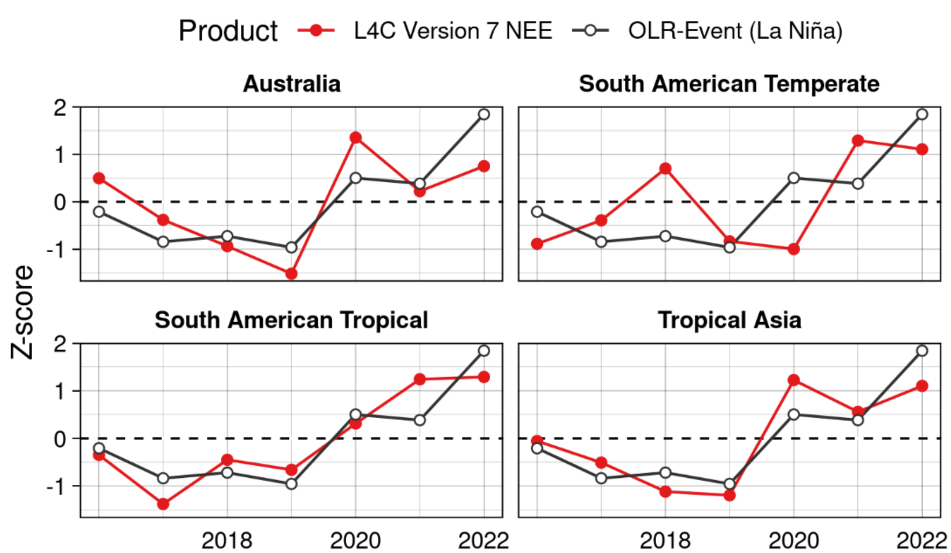

Figure 20: Annual OLR-Event (La Niña) and NEE Z-scores compared for 2015-2022.

Australia showed strong, positive (in-phase) correlations between ENSO and both GPP and R_H, suggesting both are suppressed during the warm-dry El Niño phase; the sign of the correlation with NEE suggests that GPP is suppressed (enhanced) to a greater degree than R_H by El Niño (La Niña). When correlations are computed by TransCom region (Figure 21), Australia GPP and R_H also show moderate, positive correlations (r = 0.358 for GPP using the SOI, r = 0.391 for R_H); weak anti-correlation in NEE can also be seen at the regional scale. Much of the tropics, particularly the Amazon basin, show positive correlations between NEE and ENSO, which is unexpected. This could partly be explained by a stronger land C sink in tropical drylands during the cool-wet La Niña phase (Ahlström et al. 2015). However, the South American Tropical region exhibits a moderately strong positive correlation with regionally integrated NEE (r = 0.531), driven mostly by a tight link between ENSO and R_H (r = 0.703). The OLR time series instead indicates that the recent, multi-year La Niña is associated with increased R_H in the tropics and Southern Africa, while R_H decreased during the 2015-2016 El Niño (Figure 21). Yet, it should be mentioned that a lagged spike in R_H in Southern Africa is also evident, consistent with other reports (Liu et al. 2017). Taken together, these results suggest that the impact of ENSO fluctuations on the modeled land C sink in the tropics and Southern Africa are largely due to changes in $R_{H,}$ while moisture-driven GPP fluctuations are a stronger impact in Australia. These regions are especially sensitive to ENSO fluctuations of the Central Pacific region (Dannenberg et al. 2021).

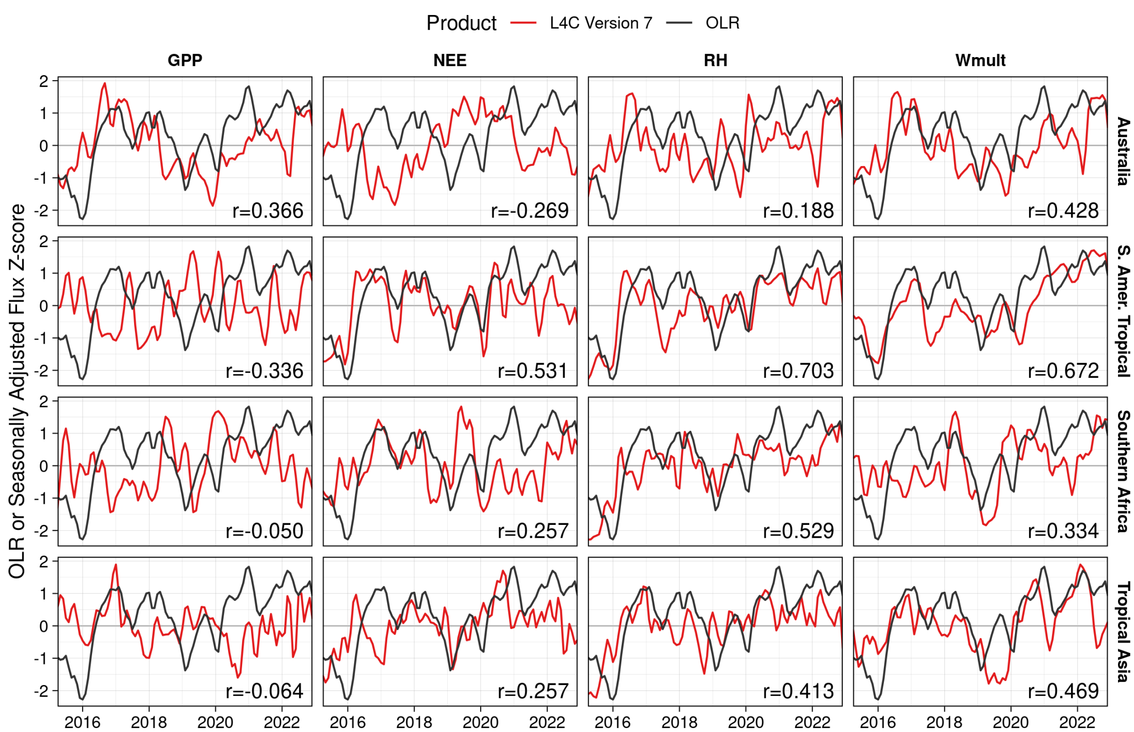

Figure 21: L4_C V7 seasonally adjusted Z-scores (red lines) of GPP, NEE, R_H, and W_{mult} (columns) by TransCom region (rows) compared to the global Outgoing Longwave Radiation (OLR) index (black line) for April 2015-December 2022. Pearson correlation coefficients (r) are shown in the bottom right of each subplot. A 2-month, low-pass, moving-window filter was applied to all time series for clarity of the display; Pearson correlations are computed from the raw (unsmoothed) data.

7 Summary and Potential Future L4_C Product Updates

Based on the multiple assessments described here, the L4_C V7 product continues to provide a level of performance and accuracy consistent with the product's science objectives. The L4_C estimated global carbon budget shows mean annual GPP and NEE fluxes that are consistent with independent estimates, while the estimated seasonal cycle and interannual variability are also comparable to independent reference datasets. L4_C simulated NEE and SOC display the expected sensitivity to short-term climatic variation, as evaluated by our comparisons to recent ENSO events and some reported extreme weather events. The relatively short record of L4_C limits our analysis, while the global extent of the product obliges us to use broad-scale climate indices and reports for comparison. The slight (not statistically significant) increase in V7 NEE RMSE compared to the previous version is largely due to the unavoidable change in fPAR source data. The L4_C product continues to exceed the targeted accuracy requirements for NEE (mean RMSE ≤ 1.6 g C m^{-2} d^{-1}) and continues to show favorable accuracy for GPP and RECO.

Future releases of the SMAP L4_C operational product will incorporate ongoing refinements and improvements to upstream inputs, including in the L4_SM algorithm. In addition, there are multiple options to improve the realism and performance of the L4_C algorithm, based on the assessments conducted here:

- Currently, L4_C is calibrated on EC tower flux data from the FLUXNET2015 and La Thuile datasets, which are only available through 2017. New EC tower flux data are available in the northern hemisphere from the NSF Arctic Data Center and individual Principal Investigators. Incorporating the CO_2 fluxes from these sites into the L4_C calibration dataset should improve model fit and the simulated carbon-cycle response to recent climatic variation. Some of the sites may also be located in deciduous needleleaf forests, which are under-represented in the current calibration dataset.
- Performance in peatlands and other regions with seasonal soil saturation could be enhanced by adding an upper limit on the response of R_H to soil moisture, effectively representing how limited soil O_2 diffusion constrains microbial respiration. We have previously evaluated the impact of this limitation on L4_C R_H and RECO performance but have not found an improvement when compared to available EC tower flux data. But more recent work (Endsley et al. 2022) suggests that some form of an O_2 diffusion limitation can improve the L4_C soil decomposition and R_H model. New tower data and the use of a second linear ramp function on the response of R_H to increasing soil moisture, rather than a quadratic curve (as used previously), could improve model performance.
- Currently, litterfall in L4_C is a fixed fraction of the annual, climatological NPP in each pixel. This assumption makes for easy model representation but ignores real seasonal variation in C inputs to soil, particularly in deciduous forests and grasslands where there is strong seasonal variation in leaf shedding. L4_C could be

more useful as a prior for atmospheric inversions if it instead used a litterfall schedule based on satellite-observed leaf-area index (Endsley et al. 2022), which is included as part of the input fPAR dataset (VIIRS VNP15A2H).

- As indicated in this assessment, the plant carbon use efficiency (CUE, or the NPP:GPP ratio) is likely too high in L4_C V7. CUE has been elevated in previous versions of L4_C as well, suggesting a persistent model bias, despite reasonable bounds on this value during calibration. Reducing CUE could help to reduce the high R_H bias as well, as any reduction in CUE must be accompanied by an increase in autotrophic respiration. Several studies and datasets are now available describing the global variation of CUE with plant traits. We could either fix optimal CUE values for each PFT or use an environmental filtering approach, where plant CUE is a function of bioclimatic covariates.

8 Acknowledgements

Funding for this work was provided by the NASA Soil Moisture Active Passive (SMAP) mission. Computing resources were provided by the NASA Center for Climate Simulation (NCCS). This work used eddy covariance data acquired by the FLUXNET community, which was supported by the CarboEuropeIP, CSIRO, FAO-GTOS-TCO, iLEAPS, Max Planck Institute for Biogeochemistry, National Science Foundation, National Research Infrastructure for Australia, Terrestrial Ecosystem Research Network, University of Tuscia, Université Laval and Environment Canada, US Department of Energy and NOAA ESRL, as well as many local funders including the Global Change Research Centre AS Czech Republic, Wisconsin Focus on Energy, and Forest Department of the Autonomous Province of Bolzano – CO_2-measuring station of Renon/Ritten. We thank Drs. A.E. Andrews, M. Aurela, D. Baldocchi, J. Beringer, P. Bolstad, J. Cleverly, B.D. Cook, K.J. Davis, A.R. Desai, D. Eamus, E. Euskirchen, J. Goodrich, L. Hutley, A. Kalhori, H. Kwon, B. Law, C. Macfarlane, W. Oechel, S. Prober, K. Rautiainen, R. Scott, H. Wheater, D. Zona and many other PIs for sharing their flux tower data.

9 References

Ahlström, A., M. R. Raupach, G. Schurgers, B. Smith, A. Arneth, M. Jung, M. Reichstein, J. G. Canadell, P. Friedlingstein, A. K. Jain, E. Kato, B. Poulter, S. Sitch, B. D. Stocker, N. Viovy, Y. P. Wang, A. Wiltshire, S. Zaehle, and N. Zeng. 2015. The dominant role of semi-arid ecosystems in the trend and variability of the land CO2 sink. *Science* 348 (6237):895–899.

Alton, P. B., R. Ellis, S. O. Los, and P. R. North. 2007. Improved global simulations of gross primary product based on a separate and explicit treatment of diffuse and direct sunlight. *Journal of Geophysical Research: Atmospheres* 112 (D7).

Anchang, J. Y., L. Prihodko, A. T. Kaptué, C. W. Ross, W. Ji, S. S. Kumar, B. Lind, M. A. Sarr, A. A. Diouf, and N. P. Hanan. 2019. Trends in woody and herbaceous vegetation in the savannas of west africa. *Remote Sensing* 11 (5):576.

Australia Bureau of Meteorology. 2021. Annual climate statement 2020. Australian government - bureau of meteorology.

Badgley, G., L. D. L. Anderegg, J. A. Berry, and C. B. Field. 2019. Terrestrial gross primary production: Using NIRV to scale from site to globe. *Global Change Biology* 25 (11):3731–3740.

Baker, D. F., R. M. Law, K. R. Gurney, P. Rayner, P. Peylin, A. S. Denning, P. Bousquet, L. Bruhwiler, Y. H. Chen, P. Ciais, I. Y. Fung, M. Heimann, J. John, T. Maki, S. Maksyutov, K. Masarie, M. Prather, B. Pak, S. Taguchi, and Z. Zhu. 2006. TransCom 3 inversion intercomparison: Impact of transport model errors on the interannual variability of regional CO2 fluxes, 1988-2003. *Global Biogeochemical Cycles* 20 (1).

Baldocchi, D. 2008. 'Breathing' of the terrestrial biosphere: Lessons learned from a global network of carbon dioxide flux measurement systems. *Australian Journal of Botany* 56 (1):1.

Bastos, A., P. Friedlingstein, S. Sitch, C. Chen, A. Mialon, J.-P. Wigneron, V. K. Arora, P. R. Briggs, J. G. Canadell, P. Ciais, F. Chevallier, L. Cheng, C. Delire, V. Haverd, A. K. Jain, F. Joos, E. Kato, S. Lienert, D. Lombardozzi, J. R. Melton, R. Myneni, J. E. M. S. Nabel, J. Pongratz, B. Poulter, C. Rödenbeck, R. Séférian, H. Tian, C. van Eck, N. Viovy, N. Vuichard, A. P. Walker, A. Wiltshire, J. Yang, S. Zaehle, N. Zeng, and D. Zhu. 2018. Impact of the 2015/2016 el niño on the terrestrial carbon cycle constrained by bottom-up and top-down approaches. *Philosophical Transactions of the Royal Society B: Biological Sciences* 373 (1760):20170304.

Bastos, A., S. W. Running, C. Gouveia, and R. M. Trigo. 2013. The global NPP dependence on ENSO: La niña and the extraordinary year of 2011: GLOBAL NPP AND ENSO: THE 2011 LA NIÑA. *Journal of Geophysical Research: Biogeosciences* 118 (3):1247–1255.

Beer, C., M. Reichstein, E. Tomelleri, P. Ciais, M. Jung, N. Carvalhais, C. Rödenbeck, M. A. Arain, D. Baldocchi, G. B. Bonan, A. Bondeau, A. Cescatti, G. Lasslop, A. Lindroth, M. Lomas, S. Luyssaert, H. Margolis, K. W. Oleson, O. Roupsard, E. Veenendaal, N. Viovy, C. Williams, F. I. Woodward, and D. Papale. 2010. Terrestrial gross carbon dioxide uptake: Global distribution and covariation with climate. *Science* 329 (5993):834–838.

Bi, W., W. He, Y. Zhou, W. Ju, Y. Liu, Y. Liu, X. Zhang, X. Wei, and N. Cheng. 2022. A global 0.05° dataset for gross primary production of sunlit and shaded vegetation canopies from 1992 to 2020. *Scientific Data* 9 (1):213.

Bond-Lamberty, B., V. L. Bailey, M. Chen, C. M. Gough, and R. Vargas. 2018. Globally rising soil heterotrophic respiration over recent decades. *Nature* 560 (7716):80–83.

Cagnarini, C., E. Blyth, B. A. Emmett, C. D. Evans, R. I. Griffiths, A. Keith, L. Jones, I. Lebron, N. P. McNamara, J. Puissant, S. Reinsch, D. A. Robinson, E. C. Rowe, A. R. C. Thomas, S. M. Smart, J. Whitaker, and B. J. Cosby. 2019. Zones of influence for soil organic matter dynamics: A conceptual framework for data and models. *Global Change Biology* 25 (12):3996–4007.

Cai, W., M. J. McPhaden, A. M. Grimm, R. R. Rodrigues, A. S. Taschetto, R. D. Garreaud, B. Dewitte, G. Poveda, Y.-G. Ham, A. Santoso, B. Ng, W. Anderson, G. Wang, T. Geng, H.-S. Jo, J. A. Marengo, L. M. Alves, M. Osman, S. Li, L. Wu, C. Karamperidou, K. Takahashi, and C. Vera. 2020. Climate impacts of the el niño–southern oscillation on south america. *Nature Reviews Earth & Environment* 1 (4):215–231.

Cai, W., W. Yuan, S. Liang, S. Liu, W. Dong, Y. Chen, D. Liu, and H. Zhang. 2014. Large differences in terrestrial vegetation production derived from satellite-based light use efficiency models. *Remote Sensing* 6 (9):8945–8965.

Chen, J. M., W. Ju, P. Ciais, N. Viovy, R. Liu, Y. Liu, and X. Lu. 2019. Vegetation structural change since 1981 significantly enhanced the terrestrial carbon sink. *Nature Communications* 10 (1):4259.

Chen, J. M., G. Mo, J. Pisek, J. Liu, F. Deng, M. Ishizawa, and D. Chan. 2012. Effects of foliage clumping on the estimation of global terrestrial gross primary productivity. *Global Biogeochemical Cycles* 26 (1).

Chiodi, A. M., and D. E. Harrison. 2013. El niño impacts on seasonal u.s. Atmospheric circulation, temperature, and precipitation anomalies: The OLR-event perspective. *Journal of Climate* 26 (3):822–837.

Chiodi, A. M., and D. E. Harrison. 2015. Global seasonal precipitation anomalies robustly associated with el niño and la niña events—an OLR perspective. *Journal of Climate* 28 (15):6133–6159.

Collalti, A., and I. C. Prentice. 2019. Is NPP proportional to GPP? Waring's hypothesis 20 years on. *Tree Physiology* 39 (8):1473–1483.

Crowell, S., D. Baker, A. Schuh, S. Basu, A. R. Jacobson, F. Chevallier, J. Liu, F. Deng, L. Feng, K. McKain, A. Chatterjee, J. B. Miller, B. B. Stephens, A. Eldering, D. Crisp, D. Schimel, R. Nassar, C. W. O'Dell, T. Oda, C. Sweeney, P. I. Palmer, and D. B. A. Jones. 2019. The 2015–2016 carbon cycle as seen from OCO-2 and the global in situ network. *Atmospheric Chemistry and Physics* 19 (15):9797–9831.

Dannenberg, M. P., W. K. Smith, Y. Zhang, C. Song, D. N. Huntzinger, and D. J. P. Moore. 2021. Large-Scale reductions in terrestrial carbon uptake following central pacific el niño. *Geophysical Research Letters* 48 (7).

Dannenberg, M. P., D. Yan, M. L. Barnes, W. K. Smith, M. R. Johnston, R. L. Scott, J. A. Biederman, J. F. Knowles, X. Wang, T. Duman, M. E. Litvak, J. S. Kimball, A. P. Williams, and Y. Zhang. 2022. Exceptional heat and atmospheric dryness amplified losses of primary production during the 2020 u.s. Southwest hot drought. *Global Change Biology* 28 (16):4794–4806.

DeLucia, E. H., J. E. Drake, R. B. Thomas, and M. Gonzalez-Meler. 2007. Forest carbon use efficiency: Is respiration a constant fraction of gross primary production? *Global Change Biology* 13 (6):1157–1167.

Demarty, J., F. Chevallier, A. D. Friend, N. Viovy, S. Piao, and P. Ciais. 2007. Assimilation of global MODIS leaf area index retrievals within a terrestrial biosphere model. *Geophysical Research Letters* 34 (15).

Du, J., J. S. Kimball, J. Sheffield, I. Velicogna, M. Zhao, M. Pan, C. K. Fisher, H. E. Beck, J. D. Watts, G. A, and E. F. Wood. 2021. Synergistic satellite assessment of global vegetation health in relation to ENSO-Induced droughts and pluvials. *Journal of Geophysical Research: Biogeosciences* 126 (5).

Endsley, K. A., J. S. Kimball, and R. H. Reichle. 2022. Soil respiration phenology improves modeled phase of terrestrial net ecosystem exchange in northern hemisphere. *Journal of Advances in Modeling Earth Systems* 14 (2).

Endsley, K. A., J. S. Kimball, R. H. Reichle, and J. D. Watts. 2020. Satellite monitoring of global surface soil organic carbon dynamics using the SMAP level 4 carbon product. *Journal of Geophysical Research: Biogeosciences* 125 (12).

Endsley, K. A., M. Zhao, J. S. Kimball, and S. Devadiga. 2023. Continuity of global MODIS terrestrial primary productivity estimates in the VIIRS era using model-data fusion. *Journal of Geophysical Research: Biogeosciences*.

Fang, Y., A. M. Michalak, C. R. Schwalm, D. N. Huntzinger, J. A. Berry, P. Ciais, S. Piao, B. Poulter, J. B. Fisher, R. B. Cook, D. Hayes, M. Huang, A. Ito, A. Jain, H. Lei, C. Lu, J. Mao, N. C. Parazoo, S. Peng, D. M. Ricciuto, X. Shi, B. Tao, H. Tian, W. Wang, Y. Wei, and J. Yang. 2017. Global land carbon sink response to temperature and precipitation varies with ENSO phase. *Environmental Research Letters* 12 (6):064007.

Forkel, M., N. Carvalhais, C. Rödenbeck, R. Keeling, M. Heimann, K. Thonicke, S. Zaehle, and M. Reichstein. 2016. Enhanced seasonal CO2 exchange caused by amplified plant productivity in northern ecosystems. *Science* 351 (6274):696–699.

Friedlingstein, P., M. O'Sullivan, M. W. Jones, R. M. Andrew, J. Hauck, A. Olsen, G. P. Peters, W. Peters, J. Pongratz, S. Sitch, C. Le Quéré, J. G. Canadell, P. Ciais, R. B. Jackson, S. Alin, L. E. O. C. Aragão, A. Arneth, V. Arora, N. R. Bates, M. Becker, A. Benoit-Cattin, H. C. Bittig, L. Bopp, S. Bultan, N. Chandra, F. Chevallier, L. P. Chini, W. Evans, L. Florentie, P. M. Forster, T. Gasser, M. Gehlen, D. Gilfillan, T. Gkritzalis, L. Gregor, N. Gruber, I. Harris, K. Hartung, V. Haverd, R. A. Houghton, T.

Ilyina, A. K. Jain, E. Joetzjer, K. Kadono, E. Kato, V. Kitidis, J. I. Korsbakken, P. Landschützer, N. Lefèvre, A. Lenton, S. Lienert, Z. Liu, D. Lombardozzi, G. Marland, N. Metzl, D. R. Munro, J. E. M. S. Nabel, S.-I. Nakaoka, Y. Niwa, K. O'Brien, T. Ono, P. I. Palmer, D. Pierrot, B. Poulter, L. Resplandy, E. Robertson, C. Rödenbeck, J. Schwinger, R. Séférian, I. Skjelvan, A. J. P. Smith, A. J. Sutton, T. Tanhua, P. P. Tans, H. Tian, B. Tilbrook, G. van der Werf, N. Vuichard, A. P. Walker, R. Wanninkhof, A. J. Watson, D. Willis, A. J. Wiltshire, W. Yuan, X. Yue, and S. Zaehle. 2020. Global carbon budget 2020. *Earth System Science Data* 12 (4):3269–3340.

Harper, A. B., P. M. Cox, P. Friedlingstein, A. J. Wiltshire, C. D. Jones, S. Sitch, L. M. Mercado, M. Groenendijk, E. Robertson, J. Kattge, G. Bönisch, O. K. Atkin, M. Bahn, J. Cornelissen, Ü. Niinemets, V. Onipchenko, J. Peñuelas, L. Poorter, P. B. Reich, N. A. Soudzilovskaia, and P. van Bodegom. 2016. Improved representation of plant functional types and physiology in the joint UK land environment simulator (JULES v4.2) using plant trait information. *Geoscientific Model Development* 9 (7):2415–2440.

Hashimoto, H., R. R. Nemani, M. A. White, W. M. Jolly, S. C. Piper, C. D. Keeling, R. B. Myneni, and S. W. Running. 2004. El niño-southern oscillation-induced variability in terrestrial carbon cycling. *Journal of Geophysical Research: Atmospheres* 109 (D23).

He, L., B. Byrne, Y. Yin, J. Liu, and C. Frankenberg. 2022. Remote-sensing derived trends in gross primary production explain increases in the CO2 seasonal cycle amplitude. *Global Biogeochemical Cycles* 36 (9).

Hengl, T., J. M. De Jesus, G. B. M. Heuvelink, M. R. Gonzalez, M. Kilibarda, A. Blagotić, W. Shangguan, M. N. Wright, X. Geng, B. Bauer-Marschallinger, M. A. Guevara, R. Vargas, R. A. MacMillan, N. H. Batjes, J. G. B. Leenaars, E. Ribeiro, I. Wheeler, S. Mantel, and B. Kempen. 2017. SoilGrids250m: Global gridded soil information based on machine learning. *PLoS ONE* 12 (2):1–40.

Holmgren, M., M. Scheffer, E. Ezcurra, J. R. Gutiérrez, and G. M. J. Mohren. 2001. El niño effects on the dynamics of terrestrial ecosystems. *Trends in Ecology & Evolution* 16 (2):89–94.

Hu, L., A. E. Andrews, K. W. Thoning, C. Sweeney, J. B. Miller, A. M. Michalak, E. Dlugokencky, P. P. Tans, Y. P. Shiga, M. Mountain, T. Nehrkorn, S. A. Montzka, K. McKain, J. Kofler, M. Trudeau, S. E. Michel, S. C. Biraud, M. L. Fischer, D. E. J. Worthy, B. H. Vaughn, J. W. C. White, V. Yadav, S. Basu, and I. R. van der Velde. 2019. Enhanced north american carbon uptake associated with el niño. *Science Advances* 5 (6):eaaw0076.

Huang, M., J. H. Crawford, G. R. Carmichael, K. W. Bowman, S. V. Kumar, and C. Sweeney. 2022. Satellite soil moisture data assimilation impacts on modeling weather variables and ozone in the southeastern US – part 2: Sensitivity to dry-deposition parameterizations. *Atmospheric Chemistry and Physics* 22 (11):7461–7487.

Jacobson, A. R., K. N. Schuldt, P. Tans, A. Andrews, J. B. Miller, T. Oda, J. Mund, B. Weir, L. Ott, T. Aalto, J. B. Abshire, K. Aikin, S. Aoki, F. Apadula, S. Arnold, B. Baier, J. Bartyzel, A. Beyersdorf, T. Biermann, S. C. Biraud, H. Boenisch, G. Brailsford, W. A. Brand, G. Chen, H. Chen, L. Chmura, S. Clark, A. Colomb, R. Commane, S. Conil, C. Couret, A. Cox, P. Cristofanelli, E. Cuevas, R. Curcoll, B. Daube, K. J. Davis, S. De Wekker, J. D. Coletta, M. Delmotte, E. DiGangi, J. P. DiGangi, A. G. Di Sarra, E. Dlugokencky, J. W. Elkins, L. Emmenegger, S. Fang, M. L. Fischer, G. Forster, A. Frumau, M. Galkowski, L. V. Gatti, T. Gehrlein, C. Gerbig, F. Gheusi, E. Gloor, V. Gomez-Trueba, D. Goto, T. Griffis, S. Hammer, C. Hanson, L. Haszpra, J. Hatakka, M. Heimann, M. Heliasz, A. Hensen, O. Hermansen, E. Hintsa, J. Holst, V. Ivakhov, D. A. Jaffe, A. Jordan, W. Joubert, A. Karion, S. R. Kawa, V. Kazan, R. F. Keeling, P. Keronen, T. Kneuer, P. Kolari, K. Komínková, E. Kort, E. Kozlova, P. Krummel, D. Kubistin, C. Labuschagne, D. H. Y. Lam, X. Lan, R. L. Langenfelds, O. Laurent, T. Laurila, T. Lauvaux, J. Lavric, B. E. Law, J. Lee, O. S. M. Lee, I. Lehner, K. Lehtinen, et al. 2023. CarbonTracker CT2022.

Jiang, M., L. Jia, M. Menenti, and Y. Zeng. 2022. Understanding spatial patterns in the drivers of greenness trends in the sahel-sudano-guinean region. *Big Earth Data*:1–20.

Johnson, S. G. 2023. *The NLopt nonlinear-optimization package*. http://github.com/stevengj/nlopt.

Joiner, J., Y. Yoshida, A. P. Vasilkov, K. Schaefer, M. Jung, L. Guanter, Y. Zhang, S. Garrity, E. M. Middleton, K. F. Huemmrich, L. Gu, and L. Belelli Marchesini. 2014. The seasonal cycle of satellite chlorophyll fluorescence observations and its relationship to vegetation phenology and ecosystem atmosphere carbon exchange. *Remote Sensing of Environment* 152:375–391.

Joiner, J., Y. Yoshida, Y. Zhang, G. Duveiller, M. Jung, A. Lyapustin, Y. Wang, and C. J. Tucker. 2018. Estimation of terrestrial global gross primary production (GPP) with satellite data-driven models and eddy covariance flux data. *Remote Sensing* 10 (9):1346.

Jones, L. A., J. S. Kimball, R. H. Reichle, N. Madani, J. Glassy, J. V. Ardizzone, A. Colliander, J. Cleverly, A. R. Desai, D. Eamus, E. S. Euskirchen, L. Hutley, C. Macfarlane, and R. L. Scott. 2017. The SMAP level 4 carbon product for monitoring ecosystem land-atmosphere CO2 exchange. *IEEE Transactions on Geoscience and Remote Sensing* 55 (11):6517–6532.

Jung, M., M. Reichstein, H. A. Margolis, A. Cescatti, A. D. Richardson, M. A. Arain, A. Arneth, C. Bernhofer, D. Bonal, J. Chen, D. Gianelle, N. Gobron, G. Kiely, W. Kutsch, G. Lasslop, B. E. Law, A. Lindroth, L. Merbold, L. Montagnani, E. J. Moors, D. Papale, M. Sottocornola, F. Vaccari, and C. Williams. 2011. Global patterns of land-atmosphere fluxes of carbon dioxide, latent heat, and sensible heat derived from eddy covariance, satellite, and meteorological observations. *Journal of Geophysical Research: Biogeosciences* 116 (G3).

Kimball, J. S., L. A. Jones, and J. P. Glassy. 2014. *Algorithm theoretical basis document SMAP level 4 carbon data product (l4_C)*. NASA Jet Propulsion Laboratory (JPL). https://smap.jpl.nasa.gov/system/internal_resources/details/original/271_L4_C_RevA_web.pdf.

Koffi, E. N., P. J. Rayner, M. Scholze, and C. Beer. 2012. Atmospheric constraints on gross primary productivity and net ecosystem productivity: Results from a carbon-cycle data assimilation system. *Global Biogeochemical Cycles* 26 (1).

Konings, A. G., A. Anthony Bloom, J. Liu, N. C. Parazoo, D. S. Schimel, and K. W. Bowman. 2019. Global satellite-driven estimates of heterotrophic respiration. *Biogeosciences* 16 (11):2269–2284.

Kraft, D. 1994. Algorithm 733: TOMP–fortran modules for optimal control calculations. *ACM Transactions on Mathematical Software* 20 (3):262–281.

Kwon, M. J., A. Ballantyne, P. Ciais, A. Bastos, F. Chevallier, Z. Liu, J. K. Green, C. Qiu, and J. S. Kimball. 2021. Siberian 2020 heatwave increased spring CO2 uptake but not annual CO2 uptake. *Environmental Research Letters* 16 (12):124030.

Lei, J., X. Guo, Y. Zeng, J. Zhou, Q. Gao, and Y. Yang. 2021. Temporal changes in global soil respiration since 1987. *Nature Communications* 12 (1):1–9.

Leroux, L., A. Bégué, D. Lo Seen, A. Jolivot, and F. Kayitakire. 2017. Driving forces of recent vegetation changes in the sahel: Lessons learned from regional and local level analyses. *Remote Sensing of Environment* 191:38–54.

Li, H., and Y. D. Wei. 2020. Spatial inequality of housing value changes since the financial crisis. *Applied Geography* 115 (December 2019):102141.

Li, X., and J. Xiao. 2019. Mapping photosynthesis solely from solar-induced chlorophyll fluorescence: A global, fine-resolution dataset of gross primary production derived from OCO-2. *Remote Sensing* 11 (21):2563.

Liu, R., R. Shang, Y. Liu, and X. Lu. 2017. Global evaluation of gap-filling approaches for seasonal NDVI with considering vegetation growth trajectory, protection of key point, noise resistance and curve stability. *Remote Sensing of Environment* 189:164–179.

Liu, Z., J. S. Kimball, N. C. Parazoo, A. P. Ballantyne, W. J. Wang, N. Madani, C. G. Pan, J. D. Watts, R. H. Reichle, O. Sonnentag, P. Marsh, M. Hurkuck, M. Helbig, W. L. Quinton, D. Zona, M. Ueyama, H. Kobayashi, and E. S. Euskirchen. 2020. Increased high-latitude photosynthetic carbon gain offset by respiration carbon loss during an anomalous warm winter to spring transition. *Global Change Biology* 26 (2):682–696.Madani, N., J. S. Kimball, A. P. Ballantyne, D. L. R. Affleck, P. M. van Bodegom, P.

B. Reich, J. Kattge, A. Sala, M. Nazeri, M. O. Jones, M. Zhao, and S. W. Running. 2018. Future global productivity will be affected by plant trait response to climate. *Scientific Reports* 8 (1):2870.

Madani, N., N. C. Parazoo, J. S. Kimball, A. P. Ballantyne, R. H. Reichle, M. Maneta, S. Saatchi, P. I. Palmer, Z. Liu, and T. Tagesson. 2020. Recent amplified global gross primary productivity due to temperature increase is offset by reduced productivity due to water constraints. *AGU Advances* 1 (4).

Mao, J., A. Ribes, B. Yan, X. Shi, P. E. Thornton, R. Séférian, P. Ciais, R. B. Myneni, H. Douville, S. Piao, Z. Zhu, R. E. Dickinson, Y. Dai, D. M. Ricciuto, M. Jin, F. M. Hoffman, B. Wang, M. Huang, and X. Lian. 2016. Human-induced greening of the northern extratropical land surface. *Nature Climate Change* 6 (10):959–963.

Mao, J., P. E. Thornton, X. Shi, M. Zhao, and W. M. Post. 2012. Remote sensing evaluation of CLM4 GPP for the period 2000–09*. *Journal of Climate* 25 (15):5327–5342.

Naidu, D. G. T., and S. Bagchi. 2021. Greening of the earth does not compensate for rising soil heterotrophic respiration under climate change. *Global Change Biology* 27 (10):2029–2038.

NOAA. 2023. Southern oscillation index (SOI). National centers for environmental information - climate monitoring. https://www.ncei.noaa.gov/access/monitoring/enso/soi (last accessed 16 March 2023).

Noon, M. L., A. Goldstein, J. C. Ledezma, P. R. Roehrdanz, S. C. Cook-Patton, S. A. Spawn-Lee, T. M. Wright, M. Gonzalez-Roglich, D. G. Hole, J. Rockström, and W. R. Turner. 2021. Mapping the irrecoverable carbon in earth's ecosystems. *Nature Sustainability* 5 (1):37–46.

Norton, A. J., P. J. Rayner, E. N. Koffi, M. Scholze, J. D. Silver, and Y.-P. Wang. 2019. Estimating global gross primary productivity using chlorophyll fluorescence and a data assimilation system with the BETHY-SCOPE model. *Biogeosciences* 16 (15):3069–3093.

Padarian, J., U. Stockmann, B. Minasny, and A. B. McBratney. 2022. Monitoring changes in global soil organic carbon stocks from space. *Remote Sensing of Environment* 281:113260.

Parazoo, N. C., K. Bowman, J. B. Fisher, C. Frankenberg, D. B. A. Jones, A. Cescatti, Ó. Pérez-Priego, G. Wohlfahrt, and L. Montagnani. 2014. Terrestrial gross primary production inferred from satellite fluorescence and vegetation models. *Global Change Biology* 20 (10):3103–3121.

Pastorello, G., C. Trotta, E. Canfora, H. Chu, D. Christianson, Y.-W. Cheah, C. Poindexter, J. Chen, A. Elbashandy, M. Humphrey, P. Isaac, D. Polidori, A. Ribeca, C. van Ingen, L. Zhang, B. Amiro, C. Ammann, M. A. Arain, J. Ardö, T. Arkebauer, S. K. Arndt, N. Arriga, M. Aubinet, M. Aurela, D. Baldocchi, A. Barr, E. Beamesderfer, L. B. Marchesini, O. Bergeron, J. Beringer,..., C. Bernhofer, D. Berveiller, D. Billesbach, T. A. Black, P. D. Blanken, G. Bohrer, J. Boike, P. V. Bolstad, D. Bonal, J.-M. Bonnefond, D. R. Bowling, R. Bracho, J. Brodeur, C. Brümmer, N. Buchmann, B. Burban, S. P. Burns, P. Buysse, P. Cale, M. Cavagna, P. Cellier, S. Chen, I. Chini, T. R. Christensen, J. Cleverly, A. Collalti, C. Consalvo, B. D. Cook, D. Cook, C. Coursolle, E. Cremonese, P. S. Curtis, E. D'Andrea, H. da Rocha, X. Dai, K. J. Davis, B. De Cinti, A. de Grandcourt, A. De Ligne, R. C. De Oliveira, N. Delpierre, A. R. Desai, C. M. Di Bella, P. di Tommasi, H. Dolman, F. Domingo, G. Dong, S. Dore, P. Duce, E. Dufrêne, A. Dunn, J. Dušek, D. Eamus, U. Eichelmann, H. A. M. ElKhidir, W. Eugster, C. M. Ewenz, B. Ewers, D. Famulari, S. Fares, I. Feigenwinter, A. Feitz, R. Fensholt, G. Filippa, M. Fischer, J. Frank, M. Galvagno, et al. 2020. The FLUXNET2015 dataset and the ONEFlux processing pipeline for eddy covariance data. *Scientific Data* 7 (1):225.

Peñuelas, J., P. Ciais, J. G. Canadell, I. A. Janssens, M. Fernández-Martínez, J. Carnicer, M. Obersteiner, S. Piao, R. Vautard, and J. Sardans. 2017. Shifting from a fertilization-dominated to a warming-dominated period. *Nature Ecology & Evolution* 1 (10):1438–1445.

Piao, S., S. Sitch, P. Ciais, P. Friedlingstein, P. Peylin, X. Wang, A. Ahlström, A. Anav, J. G. Canadell, N. Cong, C. Huntingford, M. Jung, S. Levis, P. E. Levy, J. Li, X. Lin, M. R. Lomas, M. Lu, Y. Luo, Y. Ma, R. B. Myneni, B. Poulter, Z. Sun, T. Wang, N. Viovy, S. Zaehle, and N. Zeng. 2013. Evaluation of terrestrial carbon cycle models for their response to climate variability and to CO2 trends. *Global Change Biology* 19 (7):2117–2132.

Piao, S., X. Wang, K. Wang, X. Li, A. Bastos, J. G. Canadell, P. Ciais, P. Friedlingstein, and S. Sitch. 2020. Interannual variation of terrestrial carbon cycle: Issues and perspectives. *Global Change Biology* 26 (1):300–318.

Poulter, B., D. Frank, P. Ciais, R. B. Myneni, N. Andela, J. Bi, G. Broquet, J. G. Canadell, F. Chevallier, Y. Y. Liu, S. W. Running, S. Sitch, and G. R. van der Werf. 2014. Contribution of semi-arid ecosystems to interannual variability of the global carbon cycle. *Nature* 509 (7502):600–603.

Ray, R. L., V. P. Singh, S. K. Singh, B. S. Acharya, and Y. He. 2022. What is the impact of COVID-19 pandemic on global carbon emissions? *Science of The Total Environment* 816:151503.

Rembold, F., H. Kerdiles, G. Lemoine, and A. Perez-Hoyos. 2016. *Impact of El Niño on agriculture in southern africa for the 2015/2016 main season*. Joint Research Center, European Commission. https://publications.jrc.ec.europa.eu/repository/bitstream/JRC101044/lb-02-16-379-en-n.pdf (last accessed 23 March 2023).

Ruimy, A., G. Dedieu, and B. Saugier. 1996. TURC: A diagnostic model of continental gross primary productivity and net primary productivity. *Global Biogeochemical Cycles* 10 (2):269–285.

Ryu, Y., D. D. Baldocchi, H. Kobayashi, C. van Ingen, J. Li, T. A. Black, J. Beringer, E. van Gorsel, A. Knohl, B. E. Law, and O. Roupsard. 2011. Integration of MODIS land and atmosphere products with a coupled-process model to estimate gross primary productivity and evapotranspiration from 1 km to global scales. *Global Biogeochemical Cycles* 25 (4).

Sasai, T., K. Okamoto, T. Hiyama, and Y. Yamaguchi. 2007. Comparing terrestrial carbon fluxes from the scale of a flux tower to the global scale. *Ecological Modelling* 208 (2):135–144.

Schimel, D., R. Pavlick, J. B. Fisher, G. P. Asner, S. Saatchi, P. Townsend, C. Miller, C. Frankenberg, K. Hibbard, and P. Cox. 2015. Observing terrestrial ecosystems and the carbon cycle from space. *Global Change Biology* 21 (5):1762–1776.

Still, C. J., J. A. Berry, G. J. Collatz, and R. S. DeFries. 2003. Global distribution of C3 and C4 vegetation: Carbon cycle implications. *Global Biogeochemical Cycles* 17 (1):6–1–6–14.

Tagesson, T., F. Tian, G. Schurgers, S. Horion, R. Scholes, A. Ahlström, J. Ardö, A. Moreno, N. Madani, S. Olin, and R. Fensholt. 2021. A physiology-based earth observation model indicates stagnation in the global gross primary production during recent decades. *Global Change Biology* 27 (4):836–854.

Tang, X., S. Fan, M. Du, W. Zhang, S. Gao, S. Liu, G. Chen, Z. Yu, and W. Yang. 2020. Spatial and temporal patterns of global soil heterotrophic respiration in terrestrial ecosystems. *Earth System Science Data* 12 (2):1037–1051.

Teckentrup, L., M. G. De Kauwe, A. J. Pitman, and B. Smith. 2021. Examining the sensitivity of the terrestrial carbon cycle to the expression of el niño. *Biogeosciences* 18 (6):2181–2203.

Ukkola, A., G. Abramowitz, and M. De Kauwe. 2021. A flux tower dataset tailored for land model evaluation. *Earth System Science Data Discussions*:1–20.

Wang, S., Y. Zhang, W. Ju, B. Qiu, and Z. Zhang. 2021. Tracking the seasonal and inter-annual variations of global gross primary production during last four decades using satellite near-infrared reflectance data. *Science of The Total Environment* 755:142569.

Watts, J. D., M. Farina, J. S. Kimball, L. D. Schiferl, Z. Liu, K. A. Arndt, D. Zona, A. Ballantyne, E. S. Euskirchen, F. W. Parmentier, M. Helbig, O. Sonnentag, T. Tagesson, J. Rinne, H. Ikawa, M. Ueyama, H. Kobayashi, T. Sachs, D. F. Nadeau, J. Kochendorfer, M. Jackowicz-Korczynski, A. Virkkala, M. Aurela, R. Commane, B. Byrne, L. Birch, M. S. Johnson, N. Madani, B. Rogers, J. Du, A. Endsley, K. Savage, B. Poulter, Z. Zhang, L. M. Bruhwiler, C. E. Miller, S. Goetz, and W. C. Oechel. 2023. Carbon uptake in eurasian boreal forests dominates the high-latitude net ecosystem carbon budget. *Global Change Biology*:gcb.16553.

Wei, S., C. Yi, W. Fang, and G. Hendrey. 2017. A global study of GPP focusing on light-use efficiency in a random forest regression model. *Ecosphere* 8 (5):e01724.

Wigneron, J.-P., L. Fan, P. Ciais, A. Bastos, M. Brandt, J. Chave, S. Saatchi, A. Baccini, and R. Fensholt. 2020. Tropical forests did not recover from the strong 2015–2016 el niño event. *Science Advances* 6 (6):eaay4603.

Wurster, P., M. P. Maneta, J. S. Kimball, K. A. Endsley, and S. Beguería. 2021. Monitoring crop status in the united states using the SMAP level 4 carbon product. *Frontiers in Big Data* 3.

Xu, X., J. Li, C. Wu, and A. Plaza. 2018. Regional clustering-based spatial preprocessing for hyperspectral unmixing. *Remote Sensing of Environment* 204:333–346.

Yan, H., S.-q. Wang, D. Billesbach, W. Oechel, G. Bohrer, T. Meyers, T. A. Martin, R. Matamala, R. P. Phillips, F. Rahman, Q. Yu, and H. H. Shugart. 2015. Improved global simulations of gross primary product based on a new definition of water stress factor and a separate treatment of c3 and c4 plants. *Ecological Modelling* 297:42–59.

Yan, K., J. Pu, T. Park, B. Xu, Y. Zeng, G. Yan, M. Weiss, Y. Knyazikhin, and R. B. Myneni. 2021. Performance stability of the MODIS and VIIRS LAI algorithms inferred from analysis of long time series of products. *Remote Sensing of Environment* 260:112438.

Yang, L., and M. Liu. 2023. 2021 february texas ice storm induced spring GPP reduction compensated by the higher precipitation. *Earth's Future* 11 (1).

Yebra, M., A. I. J. M. Van Dijk, R. Leuning, and J. P. Guerschman. 2015. Global vegetation gross primary production estimation using satellite-derived light-use efficiency and canopy conductance. *Remote Sensing of Environment* 163:206–216.

Yu, T., R. Sun, Z. Xiao, Q. Zhang, G. Liu, T. Cui, and J. Wang. 2018. Estimation of global vegetation productivity from global land surface satellite data. *Remote Sensing* 10 (2):327.

Yuan, W., S. Liu, G. Yu, J.-M. Bonnefond, J. Chen, K. Davis, A. R. Desai, A. H. Goldstein, D. Gianelle, F. Rossi, A. E. Suyker, and S. B. Verma. 2010. Global estimates of evapotranspiration and gross primary production based on MODIS and global meteorology data. *Remote Sensing of Environment* 114 (7):1416–1431.

Zaehle, S. 2013. Terrestrial nitrogen–carbon cycle interactions at the global scale. *Philosophical Transactions of the Royal Society B: Biological Sciences* 368 (1621):20130125.

Zhang, H., J. Bai, R. Sun, Y. Wang, Y. Pan, P. C. McGuire, and Z. Xiao. 2023. Improved global gross primary productivity estimation by considering canopy nitrogen concentrations and multiple environmental factors. *Remote Sensing* 15 (3):698.

Zhang, Y., M. P. Dannenberg, T. Hwang, and C. Song. 2019. El niño-Southern oscillation-Induced variability of terrestrial gross primary production during the satellite era. *Journal of Geophysical Research: Biogeosciences* 124 (8):2419–2431.

Zhang, Y., J. Joiner, S. Hamed Alemohammad, S. Zhou, and P. Gentine. 2018. A global spatially contiguous solar-induced fluorescence (CSIF) dataset using neural networks. *Biogeosciences* 15 (19):5779–5800.

Zhang, Y., C. Song, G. Sun, L. E. Band, S. McNulty, A. Noormets, Q. Zhang, and Z. Zhang. 2016. Development of a coupled carbon and water model for estimating global gross primary productivity and evapotranspiration based on eddy flux and remote sensing data. *Agricultural and Forest Meteorology* 223:116–131.

Zhang, Y., X. Xiao, L. Guanter, S. Zhou, P. Ciais, J. Joiner, S. Sitch, X. Wu, J. Nabel, J. Dong, E. Kato, A. K. Jain, A. Wiltshire, and B. D. Stocker. 2016. Precipitation and carbon-water coupling jointly control the interannual variability of global land gross primary production. *Scientific Reports* 6 (1):39748.

Zhao, F., and N. Zeng. 2014. Continued increase in atmospheric CO2 seasonal amplitude in the 21st century projected by the CMIP5 earth system models. *Earth System Dynamics* 5 (2):423–439.

Zheng, Y., R. Shen, Y. Wang, X. Li, S. Liu, S. Liang, J. M. Chen, W. Ju, L. Zhang, and W. Yuan. 2020. Improved estimate of global gross primary production for reproducing its long-term variation, 1982–2017. *Earth System Science Data* 12 (4):2725–2746.

Zhu, X., Y. Pei, Z. Zheng, J. Dong, Y. Zhang, J. Wang, L. Chen, R. B. Doughty, G. Zhang, and X. Xiao. 2018. Underestimates of grassland gross primary production in MODIS standard products. *Remote Sensing* 10 (11).

Zhu, Z., S. Piao, Y. Xu, A. Bastos, P. Ciais, and S. Peng. 2017. The effects of teleconnections on carbon fluxes of global terrestrial ecosystems: Effects of teleconnections on c fluxes. *Geophysical Research Letters* 44 (7):3209–3218.

Previous Volumes in This Series

Volume 1 September 1994	*Documentation of the Goddard Earth Observing System (GEOS) general circulation model - Version 1* L.L. Takacs, A. Molod, and T. Wang
Volume 2 October 1994	*Direct solution of the implicit formulation of fourth order horizontal diffusion for gridpoint models on the sphere* Y. Li, S. Moorthi, and J.R. Bates
Volume 3 December 1994	*An efficient thermal infrared radiation parameterization for use in general circulation models* M.-D. Chou and M.J. Suarez
Volume 4 January 1995	*Documentation of the Goddard Earth Observing System (GEOS) Data Assimilation System - Version 1* James Pfaendtner, Stephen Bloom, David Lamich, Michael Seablom, Meta Sienkiewicz, James Stobie, and Arlindo da Silva
Volume 5 April 1995	*Documentation of the Aries-GEOS dynamical core: Version 2* Max J. Suarez and Lawrence L. Takacs
Volume 6 April 1995	*A Multiyear Assimilation with the GEOS-1 System: Overview and Results* Siegfried Schubert, Chung-Kyu Park, Chung-Yu Wu, Wayne Higgins, Yelena Kondratyeva, Andrea Molod, Lawrence Takacs, Michael Seablom, and Richard Rood
Volume 7 September 1995	*Proceedings of the Workshop on the GEOS-1 Five-Year Assimilation* Siegfried D. Schubert and Richard B. Rood
Volume 8 March 1996	*Documentation of the Tangent Linear Model and Its Adjoint of the Adiabatic Version of the NASA GEOS-1 C-Grid GCM: Version 5.2* Weiyu Yang and I. Michael Navon

Volume 9	*Energy and Water Balance Calculations in the Mosaic LSM*
March 1996	Randal D. Koster and Max J. Suarez
Volume 10	*Dynamical Aspects of Climate Simulations Using the GEOS General Circulation Model*
April 1996	Lawrence L. Takacs and Max J. Suarez
Volume 11	*Documentation of the Tangent Linear and Adjoint Models of the Relaxed Arakawa-Schubert Moisture Parameterization Package of the NASA GEOS-1 GCM (Version 5.2)*
May 1997	Weiyu Yang, I. Michael Navon, and Ricardo Todling
Volume 12	*Comparison of Satellite Global Rainfall Algorithms*
August 1997	Alfred T.C. Chang and Long S. Chiu
Volume 13	*Interannual Variability and Potential Predictability in Reanalysis Products*
December 1997	Wie Ming and Siegfried D. Schubert
Volume 14	*A Comparison of GEOS Assimilated Data with FIFE Observations*
August 1998	Michael G. Bosilovich and Siegfried D. Schubert
Volume 15	*A Solar Radiation Parameterization for Atmospheric Studies*
June 1999	Ming-Dah Chou and Max J. Suarez
Volume 16	*Filtering Techniques on a Stretched Grid General Circulation Model*
November 1999	Lawrence Takacs, William Sawyer, Max J. Suarez, and Michael S. Fox-Rabinowitz
Volume 17	*Atlas of Seasonal Means Simulated by the NSIPP-1 Atmospheric GCM*
July 2000	Julio T. Bacmeister, Philip J. Pegion, Siegfried D. Schubert, and Max J. Suarez
Volume 18	*An Assessment of the Predictability of Northern Winter Seasonal Means with the NSIPP1 AGCM*

December 2000 — Philip J. Pegion, Siegfried D. Schubert, and Max J. Suarez

Volume 19 — *A Thermal Infrared Radiation Parameterization for Atmospheric Studies*

July 2001 — Ming-Dah Chou, Max J. Suarez, Xin-Zhong Liang, and Michael M.-H. Yan

Volume 20 — *The Climate of the FVCCM-3 Model*

August 2001 — Yehui Chang, Siegfried D. Schubert, Shian-Jiann Lin, Sharon Nebuda, and Bo-Wen Shen

Volume 21 — *Design and Implementation of a Parallel Multivariate Ensemble Kalman Filter for the Poseidon Ocean General Circulation Model*

September 2001 — Christian L. Keppenne and Michele M. Rienecker

Volume 22 — *A Coupled Ocean-Atmosphere Radiative Model for Global Ocean Biogeochemical Models*

August 2002 — Watson W. Gregg

Volume 23 — *Prospects for Improved Forecasts of Weather and Short-term Climate Variability on Subseasonal (2-Week to 2-Month) Time Scales*

November 2002 — Siegfried D. Schubert, Randall Dole, Huang van den Dool, Max J. Suarez, and Duane Waliser

Volume 24 — *Temperature Data Assimilation with Salinity Corrections: Validation for the NSIPP Ocean Data Assimilation System in the Tropical Pacific Ocean, 1993–1998*

July 2003 — Alberto Troccoli, Michele M. Rienecker, Christian L. Keppenne, and Gregory C. Johnson

Volume 25 — *Modeling, Simulation, and Forecasting of Subseasonal Variability*

December 2003 — Duane Waliser, Siegfried D. Schubert, Arun Kumar, Klaus Weickmann, and Randall Dole

Volume 26
April 2005

Documentation and Validation of the Goddard Earth Observing System (GEOS) Data Assimilation System – Version 4

Senior Authors: S. Bloom, A. da Silva and D. Dee

Contributing Authors: M. Bosilovich, J-D. Chern, S. Pawson, S. Schubert, M. Sienkiewicz, I. Stajner, W-W. Tan, and M-L. Wu

Volume 27
December 2008

The GEOS-5 Data Assimilation System - Documentation of Versions 5.0.1, 5.1.0, and 5.2.0.

M.M. Rienecker, M.J. Suarez, R. Todling, J. Bacmeister, L. Takacs, H.-C. Liu, W. Gu, M. Sienkiewicz, R.D. Koster, R. Gelaro, I. Stajner, and J.E. Nielsen

Volume 28
April 2012

The GEOS-5 Atmospheric General Circulation Model: Mean Climate and Development from MERRA to Fortuna

Andrea Molod, Lawrence Takacs, Max Suarez, Julio Bacmeister, In-Sun Song, and Andrew Eichmann

Volume 29
June 2012

Atmospheric Reanalyses – Recent Progress and Prospects for the Future.

A Report from a Technical Workshop, April 2010

Michele M. Rienecker, Dick Dee, Jack Woollen, Gilbert P. Compo, Kazutoshi Onogi, Ron Gelaro, Michael G. Bosilovich, Arlindo da Silva, Steven Pawson, Siegfried Schubert, Max Suarez, Dale Barker, Hirotaka Kamahori, Robert Kistler, and Suranjana Saha

Volume 30
December 2012

The GEOS-iODAS: Description and Evaluation

Guillaume Vernieres, Michele M. Rienecker, Robin Kovach and Christian L. Keppenne

Volume 31
March 2013

Global Surface Ocean Carbon Estimates in a Model Forced by MERRA

Watson W. Gregg, Nancy W. Casey and Cécile S. Rousseaux

Volume 32
March 2014

Estimates of AOD Trends (2002-2012) over the World's Major Cities based on the MERRA Aerosol Reanalysis

Simon Provencal, Pavel Kishcha, Emily Elhacham, Arlindo M. da Silva, and Pinhas Alpert

Volume 33

August 2014

The Effects of Chlorophyll Assimilation on Carbon Fluxes in a Global Biogeochemical Model

Cécile S. Rousseaux and Watson W. Gregg

Volume 34

September 2014

Background Error Covariance Estimation using Information from a Single Model Trajectory with Application to Ocean Data Assimilation into the GEOS-5 Coupled Model

Christian L. Keppenne, Michele M. Rienecker, Robin M. Kovach, and Guillaume Vernieres

Volume 35

December 2014

Observation-Corrected Precipitation Estimates in GEOS-5

Rolf H. Reichle and Qing Liu

Volume 36

March 2015

Evaluation of the 7-km GEOS-5 Nature Run

Ronald Gelaro, William M. Putman, Steven Pawson, Clara Draper, Andrea Molod, Peter M. Norris, Lesley Ott, Nikki Prive, Oreste Reale, Deepthi Achuthavarier, Michael Bosilovich, Virginie Buchard, Winston Chao, Lawrence Coy, Richard Cullather, Arlindo da Silva, Anton Darmenov, Ronald M. Errico, Marangelly Fuentes, Min-Jeong Kim, Randal Koster, Will McCarty, Jyothi Nattala, Gary Partyka, Siegfried Schubert, Guillaume Vernieres, Yuri Vikhliaev, and Krzysztof Wargan

Volume 37

March 2015

Maintaining Atmospheric Mass and Water Balance within Reanalysis

Lawrence L. Takacs, Max Suarez, and Ricardo Todling

Volume 38

September 2015

The Quick Fire Emissions Dataset (QFED) – Documentation of versions 2.1, 2.2 and 2.4

Anton S. Darmenov and Arlindo da Silva

Volume 39

September 2015

Land Boundary Conditions for the Goddard Earth Observing System Model Version 5 (GEOS-5) Climate Modeling System - Recent Updates and Data File Descriptions

Sarith Mahanama, Randal Koster, Gregory Walker, Lawrence Takacs, Rolf Reichle, Gabrielle De Lannoy, Qing Liu, Bin Zhao, and Max Suarez

Volume 40

Soil Moisture Active Passive (SMAP) Project Assessment Report for the Beta-Release L4_SM Data Product

October 2015 — Rolf H. Reichle, Gabrielle J. M. De Lannoy, Qing Liu, Andreas Colliander, Austin Conaty, Thomas Jackson, John Kimball, and Randal D. Koster

Volume 41 — *GDIS Workshop Report*

October 2015 — Siegfried Schubert, Will Pozzi, Kingtse Mo, Eric Wood, Kerstin Stahl, Mike Hayes, Juergen Vogt, Sonia Seneviratne, Ron Stewart, Roger Pulwarty, and Robert Stefanski

Volume 42 — *Soil Moisture Active Passive (SMAP) Project Calibration and Validation for the L4_C Beta-Release Data Product*

November 2015 — John Kimball, Lucas Jones, Joseph Glassy, E. Natasha Stavros, Nima Madani, Rolf Reichle, Thomas Jackson, and Andreas Colliander

Volume 43 — *MERRA-2: Initial Evaluation of the Climate*

September 2015 — Michael G. Bosilovich, Santha Akella, Lawrence Coy, Richard Cullather, Clara Draper, Ronald Gelaro, Robin Kovach, Qing Liu, Andrea Molod, Peter Norris, Krzysztof Wargan, Winston Chao, Rolf Reichle, Lawrence Takacs, Yury Vikhliaev, Steve Bloom, Allison Collow, Stacey Firth, Gordon Labow, Gary Partyka, Steven Pawson, Oreste Reale, Siegfried Schubert, and Max Suarez

Volume 44 — *Estimation of the Ocean Skin Temperature using the NASA GEOS Atmospheric Data Assimilation System*

February 2016 — Santha Akella, Ricardo Todling, Max Suarez

Volume 45 — *The MERRA-2 Aerosol Assimilation*

October 2016 — C. A. Randles, A. M. da Silva, V. Buchard, A. Darmenov, P. R. Colarco, V. Aquila, H. Bian, E. P. Nowottnick, X. Pan, A. Smirnov, H. Yu, and R. Govindaraju

Volume 46 — *The MERRA-2 Input Observations: Summary and Assessment*

October 2016 — Will McCarty, Lawrence Coy, Ronald Gelaro, Albert Huang, Dagmar Merkova, Edmond B. Smith, Meta Sienkiewicz, and Krzysztof Wargan

Volume 47 — *An Evaluation of Teleconnections Over the United States in an Ensemble of AMIP Simulations with the MERRA-2 Configuration of the GEOS Atmospheric Model.*

May 2017

Allison B. Marquardt Collow, Sarith P. Mahanama, Michael G. Bosilovich, Randal D. Koster, and Siegfried D. Schubert

Volume 48
July 2017

Description of the GMAO OSSE for Weather Analysis Software Package: Version 3

Ronald M. Errico, Nikki C. Prive, David Carvalho, Meta Sienkiewicz, Amal El Akkraoui, Jing Guo, Ricardo Todling, Will McCarty, William M. Putman, Arlindo da Silva, Ronald Gelaro, and Isaac Moradi

Volume 49
March 2018

Preliminary Evaluation of Influence of Aerosols on the Simulation of Brightness Temperature in the NASA Goddard Earth Observing System Atmospheric Data Assimilation System

Jong Kim, Santha Akella, Will McCarty, Ricardo Todling, and Arlindo M. da Silva

Volume 50
March 2018

The GMAO Hybrid Ensemble-Variational Atmospheric Data Assimilation System: Version 2.0

Ricardo Todling and Amal El Akkraoui

Volume 51
July 2018

The Atmosphere-Ocean Interface Layer of the NASA Goddard Earth Observing System Model and Data Assimilation System

Santha Akella and Max Suarez

Volume 52
July 2018

Soil Moisture Active Passive (SMAP) Project Assessment Report for Version 4 of the L4_SM Data Product

Rolf H. Reichle, Qing Liu, Randal D. Koster, Joe Ardizzone, Andreas Colliander, Wade Crow, Gabrielle J. M. De Lannoy, and John Kimball

Volume 53
October 2019

Ensemble Generation Strategies Employed in the GMAO GEOS-S2S Forecast System

Siegfried Schubert, Anna Borovikov, Young-Kwon Lim, and Andrea Molod

Volume 54
August 2020

Position Estimation of Atmospheric Motion Vectors for Observation System Simulation Experiments

David Carvalho and Will McCarty

Volume 55
February 2021

A Phenomenon-Based Decomposition of Model-Based Estimates of Boreal Winter ENSO Variability

Schubert, Siegfried, Young-Kwon Lim, Andrea Molod, and Allison Collow

Volume 56
June 2021

Validation Assessment for the Soil Moisture Active Passive (SMAP) Level 4 Carbon (L4_C) Data Product Version 5

John S. Kimball, K. Arthur Endsley, Tobias Kundig, Joseph Glassy, Rolf H. Reichle, and Joseph V. Ardizzone

Volume 57
July 2021

Tendency Bias Correction in the GEOS AGCM

Yehui Chang, Siegfried Schubert, Randal Koster, and Andrea Molod

Volume 58
August 2021

Soil Moisture Active Passive (SMAP) Project Assessment Report for Version 5 of the L4_SM Data Product

Rolf H. Reichle, Qing Liu, Randal D. Koster, Joseph V. Ardizzone, Andreas Colliander, Wade Crow, Gabrielle J. M. De Lannoy, and John S. Kimball

Volume 59
November 2021

Observation-Corrected Land Surface Precipitation for the SMAP Level 4 Soil Moisture (Version 6) Product and the GEOS R21C Reanalysis

Rolf H. Reichle and Qing Liu

Volume 60
January 2022

Soil Moisture Active Passive (SMAP) Project Assessment Report for Version 6 of the L4_SM Data Product

Rolf H. Reichle, Qing Liu, Randal D. Koster, Joseph V. Ardizzone, Andreas Colliander, Wade Crow, Gabrielle J. M. De Lannoy, and John S. Kimball

Volume 61
April 2022

Validation Assessment for the Soil Moisture Active Passive (SMAP) Level 4 Carbon (L4_C) Data Product Version 6

John S. Kimball, K. Arthur Endsley, Tobias Kundig, Joseph Glassy, Rolf H. Reichle, Joseph V. Ardizzone

Volume 62
September 2022

Climate Characteristics of the Atmospheric Analysis Increments from the GEOS S2S V3 AOGCM Replayed to MERRA-2

Yehui Chang, Siegfried Schubert, Randal Koster, Andrea Molod, Young-Kwon Lim

Volume 63	*GEOS aerosol optical table calculation package GEOSmie*
October 2022	*Osku Kemppinen, Peter Colarco, Patricia Castellanos*

Volume 64	*Soil Moisture Active Passive (SMAP) Project Assessment Report for Version 7 of the L4_SM Data Product*
March 2023	*Rolf Reichle, Qing Liu, Joseph Ardizzone, Michel Bechtold, Wade Crow, Gabrielle De Lannoy, John Kimball, Randal Koster*